nature physics

SUPPLEMENTARY INFORMATION

https://doi.org/10.1038/s41567-020-0785-0

In the format provided by the authors and unedited.

Strong optical coupling through superfluid Brillouin lasing

Xin He[1,2], Glen I. Harris[1,2], Christopher G. Baker[1,2]*, Andreas Sawadsky[1], Yasmine L. Sfendla[1], Yauhen P. Sachkou[1], Stefan Forstner[1] and Warwick P. Bowen[1]

[1]ARC Centre of Excellence for Engineered Quantum Systems, The University of Queensland, St Lucia, Queensland, Australia. [2]These authors contributed equally: Xin He, Glen I. Harris, Christopher G. Baker. *e-mail: c.baker3@uq.edu.au

Strong optical coupling through superfluid Brillouin lasing - Supplementary Information

Xin He, Glen I. Harris, Christopher G. Baker, Andreas Sawadsky,
Yasmine L. Sfendla, Yauhen P. Sachkou, Stefan Forstner, Warwick P. Bowen

Contents

S1 Experimental details

S1.1 Device Fabrication

Silica microdisks are fabricated from a 500 μm-thick silicon handling wafer topped by a two-micron thick thermal oxide layer (Virginia Semiconductor). Disks are defined in the silica layer through a

combination of photolithography (AZ1518 positive resist and HMDS adhesion promoter) and hydrofluoric acid (HF) wet-etch. A subsequent XeF_2 gas-phase release selectively etches the silicon material and leaves the silica disks isolated from the substrate atop a silicon pedestal, as shown in Fig.1(b) of the main text.

Unlike in previous experimental work [1, 2], the fabricated microdisks undergo no laser reflow step to form a microtoroidal resonator, and maintain their wedged outer sidewalls. This wedge shape serves a dual purpose: beyond enhancing the optical Q (over a vertical sidewalled microdisk) by making the device less sensitive to fabrication-induced roughness [3], it also serves to deconfine the optical mode and maximize the optical field intensity at the top and bottom disk interfaces where the superfluid film resides, as shown in Fig. S1. Indeed, the value of the WGM electric field at the silica interface should be optimized in order to maximize the optomechanical coupling rate between light and superfluid [4], see section S1.4. Fabricated devices show a number of WGM families, with optical Qs in the 10^5 to low 10^7 range.

S1.2 Experimental setup

The microresonator chip is positioned inside a superfluid-tight sample chamber at the bottom of a Bluefors dilution refrigerator (base temperature 10 mK). Laser light is evanescently coupled into the microresonators via a tapered optical fiber [1]. Precise fiber positioning is achieved through Attocube nanopositioning stages. The fiber taper rests on support pads microfabricated on the chip alongside the resonators [2], in order to eliminate taper drift and fluctuations. The experimental measurements are performed with the pulse-tube cooler switched off to minimize vibrations. The sample chamber contains a small volume of alumina nanopowder in order to increase the effective chamber surface area (by ~ 10 m^2), leading to more precise film thickness control and greater film thickness stability [5]. While at base temperature, ^{4}He gas can be continuously injected from the top of the cryostat into the sample chamber through a thin capillary. This allows for varying of the film thickness, and thus in-situ tuning of the Brillouin frequency.

S1.3 Characterization of superfluid film thickness

The thickness of the superfluid film covering the microresonator can be assessed through two independent means:

- First, through the magnitude of the WGM wavelength-shift across the superfluid transition temperature. When sweeping the cryostat temperature down from 1.1 K to 0.2 K, all WGMs acquire a positive wavelength shift corresponding to the increased optical path length due to the condensation of the superfluid film on the resonator surface[1], as shown in Fig. S1. Each WGM experiences a frequency shift $\frac{G}{2\pi}\Delta x$, where $G = \frac{\partial\omega_0}{\partial x}$ is the optomechanical coupling strength describing the optical cavity angular resonance frequency shift per unit deposited superfluid film thickness on the resonator boundary Δx [4, 7]. The value of G is WGM dependent, and can be calculated through FEM modelling, as detailed in section S1.4 below. With the knowledge of G, the magnitude of the experimentally measured WGM frequency shift can be converted into a deposited film thickness.

- Second, through the Brillouin frequency. The Brillouin wavelength is imposed by the wavelength of light through $\lambda_B \approx \lambda_{\text{light}}/2$, where λ_{light} is the wavelength of light in the silica given by λ_0/n_{eff}, *i.e.* the freespace wavelength λ_0 divided by the WGM effective index. The Brillouin frequency $\Omega_B/2\pi = c_3/\lambda_B$ thus informs us on the speed of sound in the superfluid c_3, which is given by [8]:

$$c_3 = \sqrt{3\,\frac{\rho_s}{\rho}\,\frac{\alpha_{\text{vdw}}}{d^3}}. \tag{1}$$

  Here the ratio ρ_s/ρ is nearly one at the low temperature used in our experiments, $\alpha_{\text{vdw}} = 2.6 \times 10^{-24}$ m^5 s^{-2} describes the van der Waals interaction between the helium atoms in the

[1] Indeed, the magnitude of the thermo-optic shift [6] over this temperature range can be neglected.

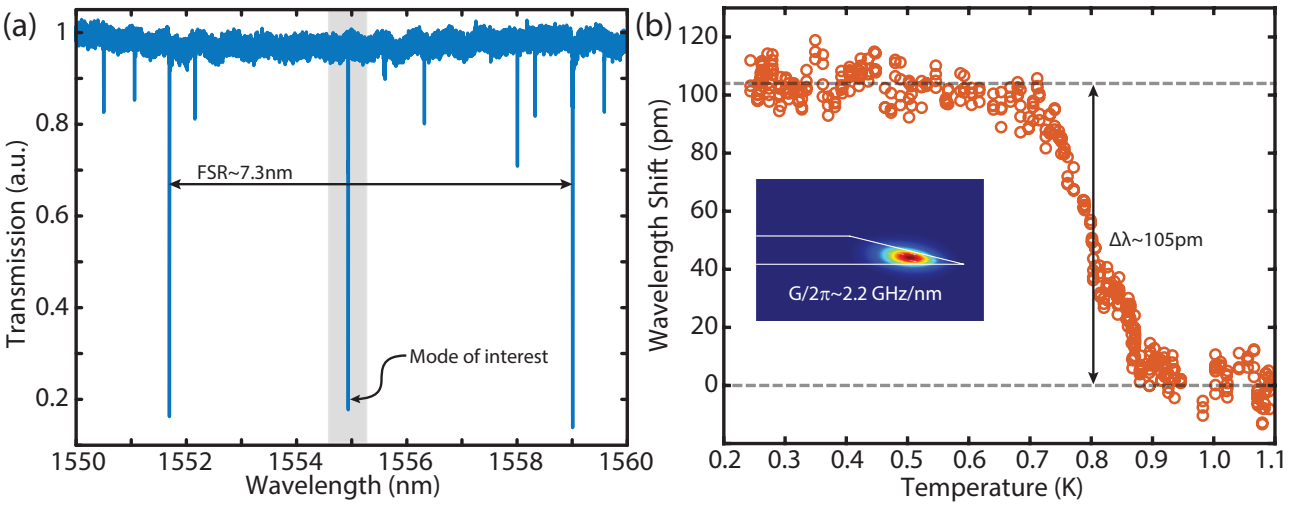

Figure S1: a) Microdisk optical spectrum, showing a number of high-Q WGMs separated by a ~ 7 nm free-spectral-range (FSR). WGM highlighted in gray near 1555 nm is the one used in the experiments. b) WGM wavelength shift as a function of fridge temperature, for the mode highlighted in (a). The vertical scatter in the data points is due to the 20 pm repeatability error in the motor sweep of our tunable laser diode. The inset displays the electric field norm of the ($p = 1$, $m_{\text{opt}} = 186$) quasi-TE mode of the structure.

superfluid and the silica disk [4] and d is the superfluid film thickness. The experimentally measured Brillouin frequency thus provides a second independent estimate of the film thickness in the experiments.

The film thickness estimation through these two methods is provided in Table S1. We ascribe the discrepancy to uncertainties in the exact device geometry. Indeed, variations in wedge angle of a few degrees can shift G by over 30%, by altering the mode confinement of the WGM and its interaction with the superfluid film. Surface roughness on the microresonator, not taken into account in the simulations, may also increase the effective surface area of the resonator and result in uncertainties in the G.

S1.4 Optomechanical coupling G

S1.4.1 Radiation-pressure contribution

We compute the optomechanical coupling strength $G = \frac{\partial \omega_0}{\partial x}$ using FEM modelling software (COMSOL Multiphysics). The silica microresonator dimensions are measured with a scanning electron microscope (SEM) and summarized in Table S1. We simulate the optical eigenmodes of the structure, which for thin disks are defined by their transverse electric (TE) or transverse magnetic (TM) polarization, and radial and azimuthal mode orders (p, m) [9]. The electric field (E) distribution of the ($p = 1$, $m = 186$) quasi-TE mode of the microdisk is plotted as an inset in Fig. S1(b). G is computed from the E field distribution through [4]:

$$G = \frac{-\omega_0}{2} \frac{\iint_{\text{interface}} (\varepsilon_{\text{sf}} - 1)\, E^2(\vec{r})\, \mathrm{d}^2\vec{r}}{\iiint_{\text{all}} \varepsilon_r(\vec{r})\, E^2(\vec{r})\, \mathrm{d}^3\vec{r}}, \tag{2}$$

where ε_r is the relative permittivity and $\varepsilon_{\text{sf}} = 1.058$ is the relative permittivity of superfluid helium[2]. The numerator surface integral is performed over both top and bottom resonator boundaries, while the normalizing denominator volume integral is performed over all space. We find values of $G/2\pi$ clustered around -2.2×10^{18} Hz/m for TE modes and around -2.4×10^{18} Hz/m for TM modes, with

[2]This simplified expression is only valid for low index-contrast interfaces, such as the one between superfluid helium $\varepsilon_{\text{sf}} = 1.058$ and vacuum $\varepsilon = 1$. In the case of high index-contrast interfaces, one must employ the expression derived by Johnson et al. [10], which properly accounts for the perpendicular E field discontinuity at the boundary.

Parameter	Symbol	Value	Units	source
Disk radius (top)	R_t	30.6	μm	SEM
Disk radius (bottom)	R_b	38.6	μm	SEM
Disk wedge angle	-	14	degrees	SEM
Film thickness	d	6	nm	Optical mode shift
		8	nm	Brillouin frequency
Speed of sound	c_3	~ 5	m/s	Eq.(1)
WGM azimuthal number	m_{opt}	186	-	FEM
Mechanical azimuthal number	m	372	-	-
Optomechanical coupling rate	$G/2\pi$	-2.17×10^{18}	Hz/m	FEM
Brillouin mode zero-point motion	x_{ZPF}	9.5×10^{-15}	m	analytical estimation
Single photon coupling strength	$g_{0,\mathrm{tot}}/2\pi$	133	kHz	Numerical fit to measurement
	$g_{0,\mathrm{rp}}/2\pi$	11	kHz	simulation
	$g_{0,\mathrm{fp}}/2\pi$	122	kHz	Numerical fit to measurement

Table S1: Experimental parameters. SEM: Scanning Electron Microscope; FEM: Finite Element Method.

little influence of the WGM radial order. Higher values of $|G|$ for TM modes is due to their stronger field at the interface due to the E field discontinuity [4]. We identify our experimental WGM as a $(p = 1, m_{\mathrm{opt}} = 186)$ quasi-TE WGM, as shown in the inset of Fig. S1(b). As mentioned above, the optomechanical coupling G has a marked dependence on the wedge angle. Indeed, while the fundamental TE mode's $|G|/2\pi \sim 2.2$ GHz/nm for a 14 degree wedge angle, this value increases to 2.5 GHz/nm for a 12 degree wedge, and drops to 1.5 GHz/nm for a 20 degree wedge angle. The contribution to the total G from top and bottom disk interfaces is well balanced, with respectively 51% and 49 % of the total coupling rate coming from top and bottom for the fundamental TE mode.

S1.4.2 Photoelastic contribution

Photoelastic contributions –resulting from the change in dielectric constant in response to strain– have been shown to be potentially appreciable in bulk superfluid helium experiments [11, 12, 13, 14]. We do not take these contributions into account however, as our acoustic wave can be well approximated by a wave in the *incompressible* limit. Indeed, the observed frequency of the Brillouin acoustic mode in our experiments is consistent with that of a third-sound wave in the incompressible limit (see section S1.6), where the restoring force is provided solely by van der Waals and capillary forces. Indeed, if the bulk modulus of liquid helium (K=8.2 MPa) were the dominant restoring force, the speed of the acoustic wave would be given by $c = \sqrt{\frac{K}{\rho}} \simeq 240$ m/s (the speed of first sound). This would lead to a characteristic Backward Brillouin frequency for 1.5 micron wavelength light upwards of 300 MHz (as for instance in Ref. [14]), far from what is observed experimentally.

S1.5 Estimation of single photon optomechanical coupling rate $g_{0,\mathrm{rp}}$

Calculation of the single-photon optomechanical coupling rate $g_{0,\mathrm{rp}} = |G|\, x_{\mathrm{ZPF}}$ [7] requires the Brillouin mode zero-point motion x_{ZPF}. The Brillouin eigenmode can be well approximated through a high-order azimuthal Bessel mode of a disk, for which the zero-point motion can be calculated analytically [4], see Fig. S2. The surface displacement η of the travelling Brillouin wave on both top and bottom surfaces of the disk is given by:

$$\eta_{m,n}\,(r,\theta,t) = \eta_0\, J_m\left(\zeta_{m,n}\frac{r}{R}\right)\cos\left(m\theta \pm \Omega_{\mathrm{B}}\, t\right), \tag{3}$$

where m and n are respectively the azimuthal and radial mode numbers, η_0 the mode amplitude, J_m the Bessel function of the first kind of order m, and $\zeta_{m,n}$ a frequency parameter depending on the mode order and the boundary conditions [4]. Energy and momentum conservation for the Brillouin scattering process imply that the Brillouin mode azimuthal order be twice that of the optical WGM,

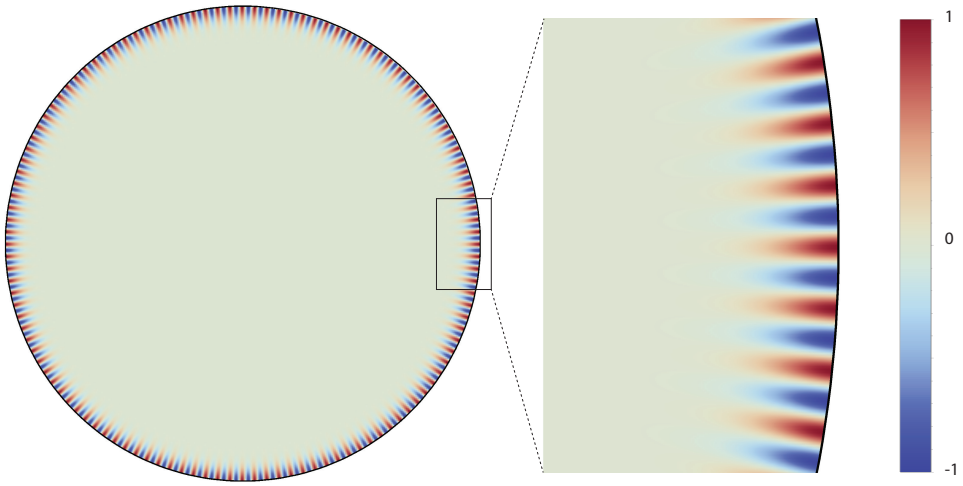

Figure S2: Example out-of-plane displacement profile of an acoustic whispering gallery-type mode (superfluid Brillouin wave) of the kind used in the experiments. For clarity, we show here the normalized displacement $\eta_{120,1}(r,\theta)$ of the $m = 120$ Bessel mode with free boundary conditions at the resonator edge [15], which has ~ 3 times fewer nodes than the experimental $m = 372$ Bessel mode. The displacement is essentially localized on the resonator edge, such that the eigenmode is not perturbed by the presence of the pedestal on the microdisk underside.

i.e. $m = 2\,m_{\rm opt} = 2 \times 186 = 372$ (see Table S1). Such a mode has its displacement localized on the periphery of the resonator, well colocalized with the optical field intensity, forming a type of acoustic whispering gallery mode, as shown in Fig. S2. Note that since the excitations exist on both the top and underside of the disk, the collective excitation of the film on top and bottom has twice the effective mass, and hence $1/\sqrt{2}$ the zero-point motion of a mode residing only on the disk top surface. The azimuthal overlap between optical and mechanical fields leads to a further factor two reduction: indeed, $\frac{1}{2\pi}\int_0^{2\pi} 2\cos^2(m_{\rm opt}\,x)\cos(m\,x)\,{\rm d}x = \frac{1}{2}$. Combined, this estimation provides, for the WGM mode used in the experiments a value of $g_{0,\rm rp} = 11$ kHz for the radiation pressure component of the single photon coupling rate. The fountain pressure contribution to the optical forcing, estimated to be $g_{0,\rm fp} = 122$ kHz from fitting to numerical simulations, arises from superfluid flow induced from optical heating [2]. As discussed in the main text, feasible improvements to the device (i.e. reduced optical and mechanical dissipation and increased optomechanical coupling through changes in disk material and thickness) can both suppress fountain pressure contributions and substantially increase radiation pressure effects, allowing the latter to dominate.

S1.6 Influence of surface tension

The dispersion relation giving the angular frequency Ω of a superfluid wave under the influence of van der Waals and surface tension restoring forces is given by:

$$\Omega = \sqrt{\frac{3\,\alpha_{\rm vdw}\,k^2}{d^3} + \frac{\sigma\,k^4\,d}{\rho}}, \tag{4}$$

where $\sigma = 3.54 \times 10^{-4}$ N/m is the superfluid ^{4}He surface tension [16] and $k = 2\pi/\lambda = \zeta_{m,n}/R$ the angular wavenumber. We plot this frequency $\Omega/2\pi$ in Fig. S3, along with the limiting cases of a pure van der Waals wave (third sound) of frequency $\Omega_{\rm vdw}/2\pi = \frac{1}{2\pi}\sqrt{\frac{3\,\alpha_{\rm vdw}\,k^2}{d^3}}$, and a pure surface tension wave (ripplon) of frequency $\Omega_\sigma/2\pi = \frac{1}{2\pi}\sqrt{\frac{\sigma\,k^4\,d}{\rho}}$. For the film thickness used in the experiment, the dominant restoring force is the van der Waals interaction, and the Brillouin wave can be well approximated by a third sound mode. For thicker films (> 13 nm), the restoring force becomes dominated by surface tension, and the wave crosses over into a ripplon-like regime.

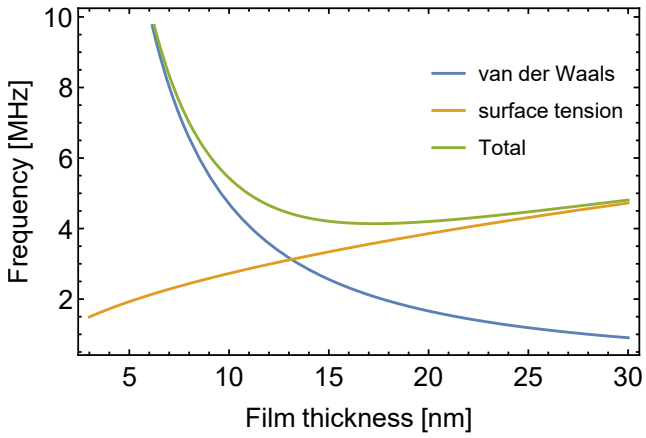

Figure S3: Frequency $\Omega_B/2\pi$ of the Brillouin wave in the presence of both van der Waals and surface tension restoring forces (green), as well as the limiting cases of the frequency $\Omega_{vdw}/2\pi$ of a pure van der Waals wave (third sound - blue) and the frequency $\Omega_\sigma/2\pi$ of a pure surface tension wave (ripplon - orange). Values plotted with $k = 10^7$, corresponding to the Brillouin wavenumber in our experiments.

S1.7 Acoustic dissipation

Thanks to its vanishing viscosity [17], superfluid helium may be employed to form extremely low dissipation mechanical oscillators. Mechanical Q factors in excess of 10^8 have been predicted and demonstrated with bulk superfluid ^{4}He resonators [18, 19]. In contrast, acoustic dissipation in superfluid helium thin films remains currently poorly understood [20, 21], and is a subject of considerable interest in its own right [22]. The superfluid third sound waves in this work display quite modest Q factors on the order of 10^2. This is more than one order of magnitude lower than observed in our previous work with superfluid-covered microtoroid resonators [1]. We ascribe the difference to two main changes. First, and likely more importantly, the resonator pedestal (see Fig. 1 of the main text) is more than one order of magnitude larger in this work compared to our previous work. This large pedestal provides a much more efficient channel for acoustic energy scattered by geometrical imperfections [23] to radiate out of the resonator, thereby playing a somewhat analogous role to increased clamping losses in nanomechanics. Second, these devices were not exposed to a final laser reflow step during their fabrication, as discussed in section S1.1. The chemically-etched wedge is therefore more rough than the nearly atomically smooth reflown silica toroids of our previous work, and any surface roughness has the potential to serve as nucleation sites for quantized vortex generation [15], as well as pinning sites for quantized vortices which may be involved in acoustic dissipation in helium films [20]. Reducing the acoustic dissipation will be addressed in future work. This may be done through improved design of the resonator's anchoring points to the environment, with for example the use of spoke-supported structures [24], or of a pedestal incorporating an acoustic shield [25]. Acoustic isolation can also be provided by opening a phononic bandgap through a periodic modulation of the superfluid wave's acoustic impedance. This can be achieved for instance through the deposition of periodically-spaced metal layers which modulate the van der Waals coefficient of the substrate upon which the superfluid waves propagate [26]. This will create a periodic modulation of the speed of sound and acoustic impedance experienced by the third sound wave –much like the approach of a Bragg mirror in optics– and allow for efficient acoustic energy reflection.

S2 Standing-wave versus travelling-wave Brillouin interaction

There has been a recent push to theoretically unify the fields of cavity optomechanics and Brillouin scattering [27]. While both fields deal with the inelastic interaction of photons with a mechanical degree of freedom (phonons), the Brillouin scattering paradigm often refers to the interaction between a travelling optical field and a travelling mechanical wave which causes a periodic refractive index modulation (see Fig. S4(a)). In contrast, the optomechanical paradigm –as illustrated by the archetypal

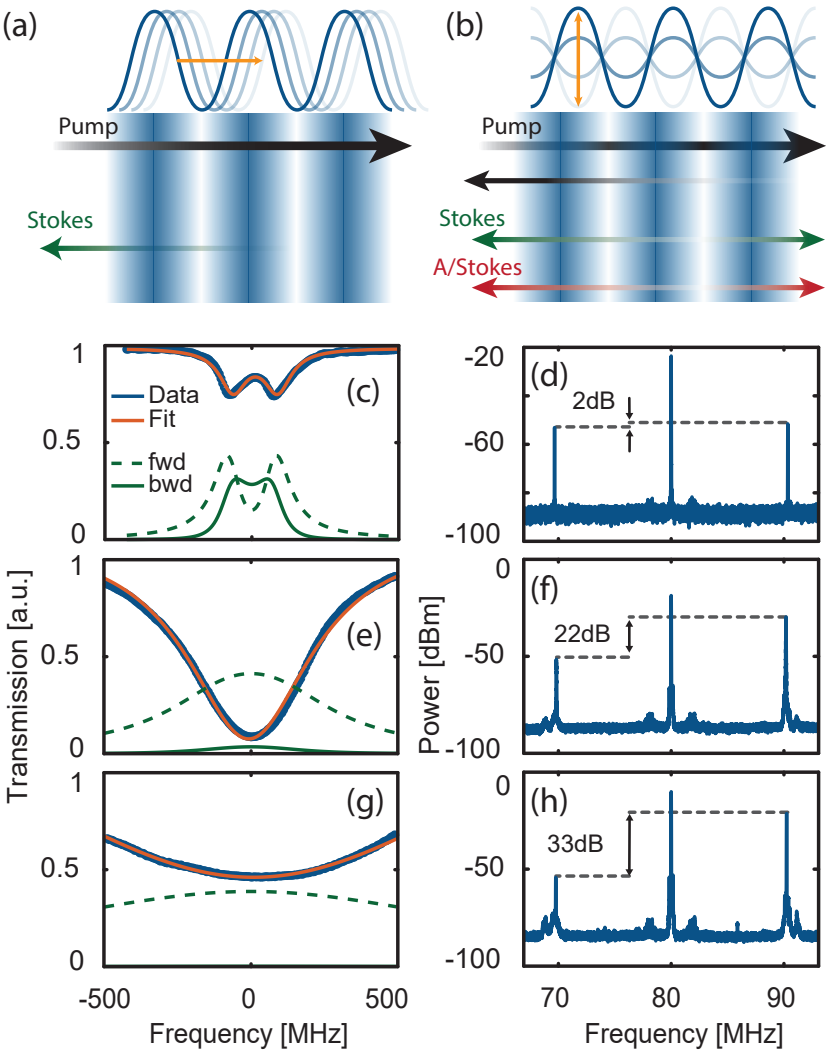

Figure S4: (a) Schematic illustration of a travelling wave 'Brillouin-like' interaction, where the pump scatters off a moving refractive index grating, leading to single Stokes sideband generation. (b) 'Optomechanics-like' interaction where the pump is scattered by a standing refractive index grating whose strength is modulated in time, leading to symmetric Stokes and anti-Stokes sideband generation. (c),(e),(g): normalized experimental WGM transmission spectra for increasing fiber taper coupling strength (blue line). The dashed and solid green lines respectively refer to the photon numbers of the forward and backward travelling directions $|a_k|^2$ and $|a_{-k}|^2$ (arbitrary units). By increasing the coupling the optical field changes from predominantly standing to predominantly travelling: $|a_k|^2/|a_{-k}|^2$ at zero detuning goes from 0.53 (c) to 11.7 (e) and 162.4 (g). (d), (f) and (h): experimental heterodyne power spectra respectively corresponding to the cases (c), (e) and (g), illustrating the transition from symmetric to asymmetric sideband generation.

Fabry-Perot cavity with a movable end-mirror– typically refers to the interaction between a standing optical field and a standing mechanical wave, as illustrated in Fig. S4(b).

We show here that these two regimes can be accessed on the same device, and that the switch can be performed in-situ, simply by tuning the position of the coupling fiber taper in order to transition from a standing to a travelling intracavity optical field. Indeed, our microresonator possesses some native optical backscattering due to geometric imperfections such as sidewall roughness, which introduces a coupling between forward and backward propagating directions. This rate is experimentally measured to be $\kappa_b = 75$ MHz, on the order of the intrinsic linewidth $\kappa_{int} = 104$ MHz, and manifests as the optical resonance taking on a characteristic doublet lineshape [28], as shown in the blue trace in Fig. S4(c).

Based on coupled-mode theory formalism (see section S2.2 below), one can compute the relative amount of light travelling in the forward and backward directions as a function of detuning in this regime, as shown in the green traces. Due to the backscattering rate κ_b being of comparable magnitude to the loss rate κ, both circulation directions are similarly populated, leading to a predominantly standing optical field, as described in Fig. S4(b). Indeed, we verify that in this regime the Stokes and anti-Stokes sidebands are comparable in magnitude, as shown in Fig. S4(d).

Next, we increase the coupling rate κ_{ext} of the cavity by approaching the fiber taper. As the cavity was previously undercoupled, this increases the depth of the transmission dip, while broadening the width of the resonance, as shown in Fig. S4(e). In this regime, the backscattering rate κ_b is no longer larger than the linewidth $\kappa = \kappa_{int} + \kappa_{ext}$, and the forward propagating field is predominantly populated (green curves), leading to a predominantly travelling optical field. This can be understood by looking at Eqs. (6) and (7) in the following, which describe the intracavity field amplitudes. Both propagation directions experience a loss rate $\kappa = \kappa_{int} + \kappa_{ext}$ which depends on κ_{ext}. However, while increasing κ_{ext} increases both the loss rate and the pump rate of the forward field (see Eq. (6)), it only increases the loss rate of the backward propagating mode, which is pumped at a fixed rate proportional to κ_b (see Eq. (7)). Increasing the coupling rate to the taper therefore biases the system towards a forward travelling optical field and a situation analogous to the Brillouin case described in Fig. S4(a). Indeed, in this coupling regime the asymmetry between Stokes and anti-Stokes sidebands reaches 22 dB, as shown in Fig. S4(f). Further increasing the taper coupling rate well into the overcoupled regime (Fig. S4(g)) leads to an even higher ratio of forward to backward optical intensity ($|a_k|^2/|a_{-k}|^2 = 162$ on resonance), and a sideband asymmetry reaching 33 dB (Fig. S4(h)).

S2.1 Hamiltonian of optical fields in the presence of backscattering

In addition to a mechanically mediated coupling (e.g. the Brillouin induced strong coupling discussed in section S7), the coupling of two WGMs can be induced by the backscattering caused by imperfections of the resonator geometry such as sidewall roughness [28]. Unlike the mechanically induced optical coupling, this type of coupling is stationary, so we define a fixed mutual coupling strength κ_b between the two optical modes a_k and a_{-k} (forward and backward propagating respectively). The Hamiltonian of the system derived from coupled mode theory is:

$$\hat{H} = \hbar\omega_k a_k^\dagger a_k + \hbar\omega_{-k} a_{-k}^\dagger a_{-k} - \hbar\kappa_b \left(a_k^\dagger a_{-k} + a_k a_{-k}^\dagger \right), \tag{5}$$

where ω_k and ω_{-k} are the bare eigen-frequencies of the two optical modes, and the associated a is the lowering operator of each mode. The subscript k is the wave number of the optical modes, with the signs in the front indicating direction of propagation. The interaction term is a beamsplitter interaction between the two optical modes. In the case of an ideal WGM resonator $\omega_k = \omega_{-k}$, but in the presence of strong backscattering (i.e. $\kappa_b >> \kappa$) the bare eigen-modes of the cavity hybridize into two distinct non-degenerate modes [28].

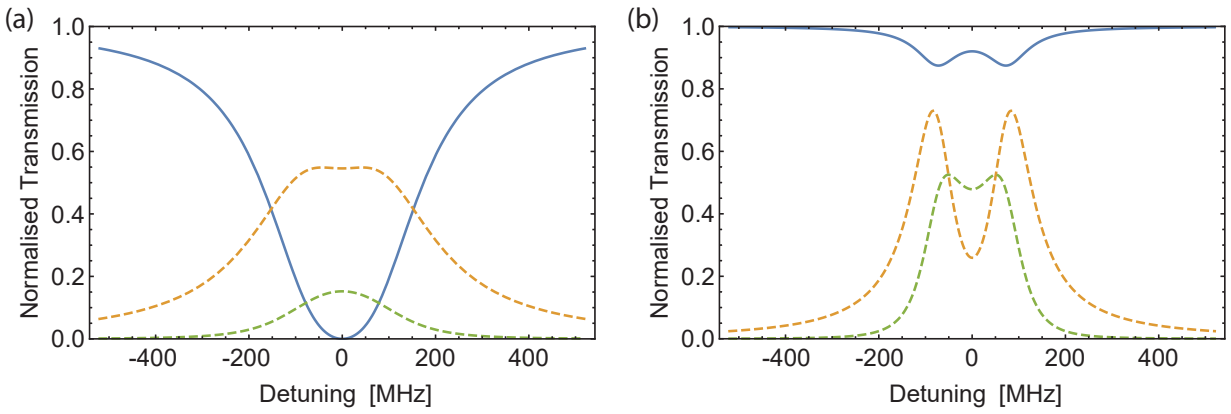

Figure S5: Normalised WGM transmission spectrum in the presence of backscattering, plotted using Eq. (10). Blue: Normalized transmission. Yellow and green dashed lines refer respectively to the forward and backward propagating field intensities $|a_k|^2$ and $|a_{-k}|^2$ in arbitrary units, obtained from Eqs (8) and (9). (a) Intrinsic optical linewidth κ_{int}: 104 MHz, taper coupling rate κ_{ext}: 180 MHz, backscattering rate κ_b: 75 MHz. (b) Undercoupled regime with intrinsic optical linewidth κ_{int}: 104 MHz, taper coupling rate κ_{ext}: 6.4 MHz, backscattering rate κ_b: 75 MHz.

S2.2 Equations of motion

Including dissipation and drive, but ignoring vacuum fluctuations, the equations of motion are obtained for the coupled optical cavity modes from the Hamiltonian of Eq.(5):

$$\dot{a}_k = i\Delta a_k - \frac{\kappa}{2}a_k + i\kappa_b a_{-k} + \sqrt{\kappa_{ext}}a_{in} \tag{6}$$

$$\dot{a}_{-k} = i\Delta a_{-k} - \frac{\kappa}{2}a_{-k} + i\kappa_b a_k, \tag{7}$$

where $\Delta = \omega_L - \omega_{k(-k)}$ is the detuning, $\kappa = \kappa_{int} + \kappa_{ext}$ is the total optical decay rate for either optical mode. κ_{ext} is the coupling rate to the tapered optical fibre, and κ_{int} is the intrinsic optical cavity decay rate. The pump field a_{in} drives the forward propagating mode a_k via the fiber taper. The amplitude of the pump field a_{in} is related to the incoming photon flux in the tapered fibre, via $|a_{in}|^2 = \frac{P_{in}}{\hbar\omega}$, with P_{in} the input laser power. Solving the equations of motion in the steady state, the forward propagating mode a_k has the solution:

$$a_k = \frac{\sqrt{\kappa_{ext}}\, a_{in}}{-i\Delta + \kappa_k/2 + \frac{\kappa_b^2}{-i\Delta+\kappa_{-k}/2}}. \tag{8}$$

The amplitude of the backscattered field a_{-k} travelling in the opposite direction can be expressed as a function of a_k:

$$a_{-k} = \frac{i\,\kappa_b\, a_k}{-i\Delta + \kappa_{-k}/2}. \tag{9}$$

Using the input-output theorem, the output light in the fibre after the cavity is a_{out}, equal to $a_{in} - \sqrt{\kappa_{ext}}\, a_k$. Thus, the normalised transmission spectrum in the fibre after the WGM cavity is:

$$\begin{aligned} T &= \left|\frac{a_{out}}{a_{in}}\right|^2 \\ &= \left|1 - \frac{\sqrt{\kappa_{ext}}a_k}{a_{in}}\right|^2 \end{aligned} \tag{10}$$

The effect of the taper coupling rate κ_{ext} on the ratio of forward to backward travelling light intensity is illustrated in Fig. S5. We consider an optical mode with an unloaded optical decay rate $\kappa_{int} = 104$ MHz, and a backscattering coupling rate $\kappa_b = 75$ MHz. When the taper coupling rate is set to $\kappa_{ext} = 180$ MHz, the resulting cavity transmission is plotted in Fig. S5(a). Because the total

dissipation rate $\kappa = \kappa_{int} + \kappa_{ext}$ is larger than κ_b, the mode splitting is not resolvable in the cavity transmission (blue curve). For the same reason, the intracavity intensity of the forward propagating optical field (dashed yellow line) is around 4 times larger than that of the field propagating in the opposite direction (dashed green line). This intensity difference of the two optical modes leads to a net forward travelling optical field in the cavity. In contrast, when the taper coupling rate is reduced such that the total dissipation rate is now comparable to the backscattering rate, the lifted degeneracy between forward and backward propagating fields is revealed, as shown in the blue transmission trace in Fig. S5(b). In this regime, both optical fields are similarly populated, resulting in a predominantly standing optical field.

S3 Orthogonality of Brillouin grating

The whispering gallery modes constitute orthogonal eigenmodes of the electromagnetic field confined inside the optical resonator. Because of this orthogonality, the superfluid surface deformation (and its associated refractive index modulation) caused by driving one WGM should in principle leave other WGMs unaffected. This is indeed what we observe in the experiments. Figure S6(a) shows a transmission spectrum of our microresonator, with the WGM used in the experiments ($m_{\text{opt}} = 186$) highlighted in red. The WGM of the same mode family with the next azimuthal order ($m_{\text{opt}}+1 = 187$), separated from the first by a free spectral range, is highlighted in green. Using the pump-probe setup described in the main text and section S7, we use the strong pump tuned to the m_{opt} WGM to initiate Brillouin lasing. In this regime, the weak probe scanned over the m_{opt} WGM reveals a doublet splitting (Fig. S6(b)), a manifestation of the strong coupling between forward and backward propagating optical fields mediated by the superfluid index grating. In contrast, sweeping over the adjacent $m_{\text{opt}}+1$ WGM in the same lasing regime shows this mode remains unaffected and maintains its Lorentzian shape, see Fig. S6(c).

A schematic illustration of this orthogonality is shown in Fig. S6(d), with lower azimuthal orders plotted here for clarity. The top panel shows the intensity profile, proportional to E^2, of the $m_{\text{opt}} = 10$ WGM along the circumference of the resonator (red), along with the associated superfluid film deformation generated by the Brillouin scattering process (blue). The lower panel shows this same surface deformation (blue) along with the field intensity of the $m_{\text{opt}} + 1 = 11$ WGM. Because of the WGM orthogonality, the refractive index modulation created by mode m_{opt} leads to net change in optical path length for the $m_{\text{opt}} + 1$ WGM, and hence no energy shift (Eq.(11)) and a zero $g_{0,\text{rp}}$ and g_{opt}, see section S7.3.

S4 Analytical theory - non-depleted pump regime

S4.1 Hamiltonian formalism

Here we detail the analytical Brillouin scattering theory, which describes the superfluid Brillouin system in the non-depleted pump regime, an approximation valid below the lasing threshold. The general interaction Hamiltonian is determined by the overlap integral of the optical and acoustic fields [29, 4]. We derive it below, based on a perturbation theory approach. The energy shift ΔE experienced by the optical field due to the presence of the superfluid is given by:

$$\Delta E = \int_{r=0}^{R} \int_{\theta=0}^{2\pi} \int_{z=0}^{d_0+\eta(r,\theta)} \frac{1}{2}\,\varepsilon_0\,(\varepsilon_{\text{sf}} - 1)\,|E|^2\,r\,\mathrm{d}r\,\mathrm{d}\theta\,\mathrm{d}z, \tag{11}$$

where $\varepsilon_0 = 8.85 \times 10^{-12}$ F/m is the vacuum permittivity, ε_{sf} is the relative permittivity of superfluid helium, η is the out-of-plane displacement of the superfluid surface beyond a mean height d_0 due to the acoustic wave (third sound), E is the WGM electric field and R is the radius of the disk resonator. Given the film thickness is only a few nanometres, the electric field can be treated as constant over the height of the film. Thus the volume integral Eq. (11) can be reduced to an integral over the surface of the disk resonator:

$$\Delta E = \int_{0}^{R} \int_{0}^{2\pi} \frac{1}{2}\,\varepsilon_0\,(\varepsilon_r - 1)\,(d_0 + \eta\,(r,\theta))\,|E|^2\,r\,\mathrm{d}r\,\mathrm{d}\theta \tag{12}$$

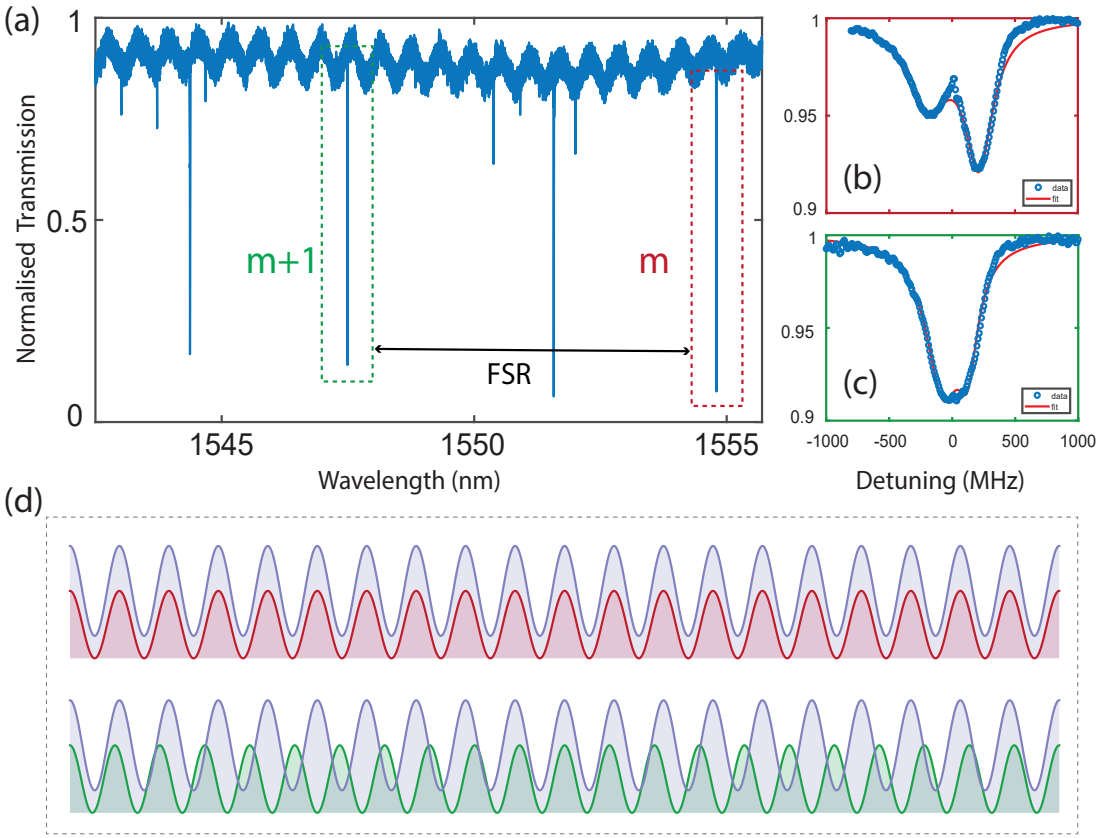

Figure S6: a) Normalized experimental cavity transmission spectrum, showing the optical mode used in the experiments ($m_{\mathrm{opt}} = 186$) near 1555 nm (dashed red box), along with the next azimuthal order WGM ($m_{\mathrm{opt}} + 1 = 187$) separated in wavelength by an FSR (dashed green box). In the presence of the strong refractive index grating created by pumping mode m_{opt} above the Brillouin lasing threshold, the pumped mode measured by the probe laser reveals strong mechanically induced optical coupling (b), while the adjacent $m_{\mathrm{opt}} + 1$ optical mode remains unsplit (c). d) Schematic illustration of mode orthogonality between mode $m_{\mathrm{opt}} = 10$ (red) and its associated refractive index modulation (blue) and mode $m_{\mathrm{opt}} + 1 = 11$ (green).

We rewrite this expression in terms of photon and phonon annihilation and creation operators:

$$\Delta E = \int_{\text{surface}} \frac{1}{2}\,\varepsilon_0\,(\varepsilon_r - 1)\left[\underbrace{\Psi_b(\vec{r})\left(b_q + b_q^\dagger + b_{-q} + b_{-q}^\dagger\right)}_{\text{AC}} + \underbrace{d_0}_{\text{DC}}\right]\left[|\Psi_a(\vec{r})|^2 |a_k + a_{-k}|^2\right]\,\mathrm{d}A. \tag{13}$$

Here $\Psi_a(\vec{r}) = E\,(\vec{r})\,\sqrt{\frac{\hbar\omega}{\int \frac{1}{2}\,\varepsilon_0\,\varepsilon_r\,E^2\,\mathrm{d}V}}$ is the electric amplitude per photon, $\Psi_b(\vec{r})$ is the acoustic amplitude in the ground state, a_k (b_q) and a_{-k} (b_{-q}) are respectively the photon (phonon) annihilation operators acting on the forward and backward propagating optical (acoustic) modes. The subscripts k (q) refer respectively to the wavenumbers of the optical (acoustic) wave and the signs in front of k and q indicate the propagation direction, with the convention that the optical pump travels in the positive direction. In the limit that the Brillouin frequency is much smaller than the optical frequency ($\Omega_{\text{B}} \ll \omega_{\text{opt}}$), momentum and energy conservations require that $q = 2k$ for the Brillouin process.

The acoustic term in Eq. (13) can be broken into two components: a DC component proportional to the mean film thickness d_0 which gives the DC shift of the optical resonance frequency due to the superfluid helium film covering the resonator, and an AC component describing the interaction of the surface acoustic wave with the intracavity optical field. Neglecting the DC part, the interaction Hamiltonian takes the form:

$$\begin{aligned} H_{\text{int}} &= -\int_{\text{surface}} \frac{1}{2}\,\varepsilon_0\,(\varepsilon_r - 1)\,\Psi_b(\vec{r})|\Psi_a(\vec{r})|^2\,\mathrm{d}A\,(b_q + b_q^\dagger + b_{-q} + b_{-q}^\dagger)|a_k + a_{-k}|^2 \\ &= -\hbar\,g_{0,\text{rp}}\,(b_q + b_q^\dagger + b_{-q} + b_{-q}^\dagger)(a_k^\dagger + a_{-k}^\dagger)(a_k + a_{-k}), \end{aligned} \tag{14}$$

where $g_{0,rp}$ is the single photon optomechanical coupling rate from radiation pressure [7, 4]:

$$g_{0,\text{rp}} = \int_{\text{surface}} \frac{1}{2}\,\varepsilon_0\,(\varepsilon_{\text{sf}} - 1)\;\Psi_b(\vec{r})\,|\Psi_a(\vec{r})|^2\;\mathrm{d}A \tag{15}$$

The interaction Hamiltonian is further reduced by energy and momentum conservation arguments to the following form:

$$H_{\text{int}} = -\hbar\,g_{0,\text{rp}}(b_q^\dagger a_k a_{-k}^\dagger + b_{-q} a_k a_{-k}^\dagger + b_{-q}^\dagger a_k^\dagger a_{-k} + b_q a_k^\dagger a_{-k}) \tag{16}$$

The first two terms correspond respectively to the Stokes and anti-Stokes scattering process for the forward propagating optical field a_k, while the third and fourth terms correspond respectively to the Stokes and anti-Stokes process acting on the counter-propagating optical field a_{-k}.

Note that in many other works [30, 31], the resonator's optical spectrum is engineered such that pump and Stokes fields are resonant with two distinct optical modes separated by the Brillouin shift. Compared with the pump and Stokes, the non-resonant anti-Stokes field experiences a very low optical density of states and can therefore be neglected. Here, because of the small Brillouin shift (~ 6 MHz), we must keep both the Stokes and anti-Stokes terms. In addition, the frequencies of the two counter-propagating optical modes are degenerate, such that the frequencies of a_k and a_{-k} are both treated as Δ in the full Hamiltonian description in a frame rotating at the laser frequency ω_L, where Δ is defined as $\omega_L - \omega_k$:

$$H = \underbrace{-\hbar\Delta a_k^\dagger a_k - \hbar\Delta a_{-k}^\dagger a_{-k}}_{\text{optical}} + \underbrace{\hbar\Omega_{\text{B}} b_q^\dagger b_q + \hbar\Omega_{\text{B}} b_{-q}^\dagger b_{-q}}_{\text{mechanical}} \underbrace{-\hbar g_{0,\text{rp}}(b_q a_k^\dagger a_{-k} + b_{-q}^\dagger a_k^\dagger a_{-k} + b_{-q} a_{-k}^\dagger a_k + b_q^\dagger a_{-k}^\dagger a_k)}_{\text{Brillouin interaction}} \tag{17}$$

S4.2 Fountain Pressure

Before deriving the equations of motion we must also consider the force applied to the superfluid film via absorption-induced entropy gradients. In a similar way to radiation pressure, the fountain pressure

is introduced as a fluctuating force, but with temporal correlations generated by the thermal response to random photon absorption events [32, 33, 34].

$$F_{fp}(t) = \hbar\, g_{0,fp}\, \frac{1}{\tau_t} \int_{-\infty}^{t} \mathrm{d}u\, e^{-\frac{t-u}{\tau_t}}\, a^{\dagger}_{-k}(u) a_k(u) \tag{18}$$

$$= \hbar\, g_{0,fp} \left(\frac{1}{\tau_t} H(t)\, e^{-\frac{t}{\tau_t}} \right) * (a^{\dagger}_{-k}(t) a_k(t)) \tag{19}$$

where τ_t is the thermal response time and $g_{0,fp}$ is the fountain pressure coupling rate which quantifies the strength of the forcing. In general, the absolute value and even the sign of $g_{0,fp}$ depends both on the ratio of absorbed to circulating optical power and the spatial overlap of the optical and mechanical modes. To go from Eq.18 to Eq.19, the integral is replaced by a convolution with an exponential decay and a Heaviside function $H(t)$ to preserve causality.

For the fountain pressure force, two distinct regimes can be realized depending on the thermalization rate τ_t. This is most easily seen by considering the force in the Fourier domain. Indeed, using the Fourier identity $\mathscr{F}\{\frac{1}{\tau_t} H(t) e^{-t/\tau_t}\} = \frac{1}{1+i\tau_t\omega}$, we see that the $a^{\dagger}_{-k} a_k$ term in Eq.19 will be filtered by a low pass filter with a corner frequency defined by the characteristic thermalization time τ_t. If τ_t is small compared to ω, corresponding to materials with high thermal conductivity, then the low pass filter approaches unity and the fountain pressure force will simply be $F_{fp}(t) = \hbar\, g_{0,fp}\, a^{\dagger}_{-k}(t) a_k(t)$. In this limit, the fountain pressure force is qualitatively indistinguishable from radiation pressure forces, provided the sign of $g_{0,fp}$ is positive. If τ_t is equal to or larger than ω, corresponding to materials with low thermal conductivity, then the low pass filter will provide both attenuation and a phase-lag. This type of thermal response (i.e. non-Markovian) will result non-trivial back-action, hence modifying the mechanical resonance frequency (i.e. frequency pulling) and dissipation (i.e. linewidth narrowing/broadening).

For the system considered here we observe minimal change in the mechanical resonance frequency when approaching the lasing threshold. This validates the assumption that $\tau_t << \Omega_B$, which is also consistent with the high thermal conductivity exhibited by superfluid helium. Furthermore, in the limit of a dominant fountain pressure force, the sign of $g_{0,fp}$ dictates which travelling acoustic wave is amplified by the Brillouin process. This contrasts from a purely radiation pressure based interaction, but is not unexpected since the fountain pressure force is intrinsically energy non-conserving, enabling the amplification of either the co-propagating or counter-propagating acoustic mode, with respect to the pump. Here, we experimentally observe amplification of the acoustic mode that co-propagates with the pump, indicating a positive sign on $g_{0,fp}$. Henceforth, we assume the fountain pressure force takes the form $F_{fp}(t) = \hbar\, g_{0,fp}\, a^{\dagger}_{-k}(t) a_k(t)$.

S4.3 Equations of motion

From this Hamiltonian we derive the equations of motion. Including the drive a_{in} of the pump field, the fountain pressure coupling ($g_{0,\mathrm{fp}} = g_{0,\mathrm{tot}} - g_{0,\mathrm{rp}}$), the native backscattering κ_b, the thermal drive b_{in} (b_{-in}) of the acoustic fields b_q (b_{-q}) respectively [31, 35] and dissipation we obtain:

$$\dot{a}_k = i\Delta a_k - \frac{\kappa}{2} a_k + i g_{0,\mathrm{rp}} (b_q a_{-k} + b^{\dagger}_{-q} a_{-k}) + i\kappa_b a_{-k} + \sqrt{\kappa_{ext}}\, a_{in} \tag{20}$$

$$\dot{a}_{-k} = i\Delta a_{-k} - \frac{\kappa}{2} a_{-k} + i g_{0,\mathrm{rp}} (b_{-q} a_k + b^{\dagger}_{q} a_k) + i\kappa_b a_k \tag{21}$$

$$\dot{b}_q = -i\Omega_{\mathrm{B}} b_q - \frac{\Gamma}{2} b_q + i g_{0,\mathrm{tot}}\, a^{\dagger}_{-k} a_k + \sqrt{\Gamma}\, b_{in}(t) \tag{22}$$

$$\dot{b}_{-q} = -i\Omega_{\mathrm{B}} b_{-q} - \frac{\Gamma}{2} b_{-q} + i g_{0,\mathrm{tot}}\, a^{\dagger}_{k} a_{-k} + \sqrt{\Gamma}\, b_{-in}(t), \tag{23}$$

where κ is the optical decay rate, κ_{ext} the coupling rate of the optical cavity to the tapered fibre, n_q (n_{-q}) the thermal occupation of the co-propagating (counter-propagating) acoustic field, Γ the intrinsic mechanical damping rate, and $b_{in}(t)$ the thermal drive, which obeys the Markovian noise process such that $\langle b^{\dagger}_{in}(t) b_{in}(t')\rangle = n_q\, \delta(t-t')$ and $\langle b_{in}(t) b^{\dagger}_{in}(t')\rangle = (n_q+1)\delta(t-t')$ [35]. Note that light

can drive the acoustic wave through both the radiation pressure and fountain pressure interactions, but the acoustic wave affects light only through thickness fluctuations, namely dispersive coupling mediated by radiation pressure.

We make the assumption that a_k is a non-depleted pump, and the native backscattered light is also not depleted. Then the equations of motion can be linearized by decomposing a_k and a_{-k} into an average coherent amplitude α_k (or α_{-k}) given by the steady state solution, and a time-variant part δa_k (or δa_{-k}) describing the dynamics of the system. First we neglect the Brillouin interaction and solve the steady-state of the pump and the backscattered light from Eq. (20) and Eq. (21), and obtain:

$$\alpha_k = \sqrt{n_{cav}} = \left| \frac{\sqrt{\kappa_{ext}}\,\alpha_{in}}{-i\Delta + \kappa/2 + \frac{\kappa_b^2}{-i\Delta+\kappa/2}} \right|, \tag{24}$$

$$\alpha_{-k} = \left| \frac{i\kappa_b}{-i\Delta + \kappa/2} \cdot \frac{\sqrt{\kappa_{ext}}\,\alpha_{in}}{-i\Delta + \kappa/2 + \frac{\kappa_b^2}{-i\Delta+\kappa/2}} \right|. \tag{25}$$

Here we define $n_{cav,k}$ and $n_{cav,-k}$ as the intracavity photon number approximated by the steady state solution of the pump and backscattered light respectively: $n_{cav,k} = |\alpha_k|^2$, $n_{cav,-k} = |\alpha_{-k}|^2$.

It is important to point out here, that the presence of weak backscattering manifests as a suppression of Brillouin amplification. This suppression arises primarily from two mechanisms: first, through the depletion of pump photons from backscattering, and second, those backscattered photons (now counter-propagating) actively cool the acoustic mode that is being amplified by the pump. Nevertheless, the lasing threshold behavior still remains qualitatively the same, albeit occuring at higher injected optical powers. To concisely describe the lasing threshold behavior the following sub-sections (Sec.S4.4 and Sec.S4.5) will neglect the effect of backscattering. However, when processing the experimental data to extract the total optomechanical coupling rate the full dynamical equations will be considered (see Sec.S5).

Subtracting the steady state solutions from Eqs.(20,21,22,23) and neglecting backscattering, optical vacuum noises and higher order terms of the time-variant variables, the Fourier transformed equations of motion are:

$$-i\omega\delta a_k(\omega) = i\Delta\delta a_k(\omega) - \frac{\kappa}{2}\delta a_k(\omega) + ig_{0,\mathrm{rp}}\alpha_{-k}(b_q(\omega) + b_{-q}^\dagger(\omega)), \tag{26}$$

$$-i\omega\delta a_{-k}(\omega) = i\Delta\delta a_{-k}(\omega) - \frac{\kappa}{2}\delta a_{-k}(\omega) + ig_{0,\mathrm{rp}}\alpha_k(b_{-q}(\omega) + b_q^\dagger(\omega)), \tag{27}$$

$$-i\omega b_q(\omega) = -i\Omega_\mathrm{B} b_q(\omega) - \frac{\Gamma}{2}b_q(\omega) + ig_{0,\mathrm{tot}}(\alpha_{-k}^*\delta a_k(\omega) + \alpha_k\delta a_{-k}^\dagger(\omega)) + \sqrt{\Gamma}\,b_{in}(\omega), \tag{28}$$

$$-i\omega b_{-q}(\omega) = -i\Omega_\mathrm{B} b_{-q}(\omega) - \frac{\Gamma}{2}b_{-q}(\omega) + ig_{0,\mathrm{tot}}(\alpha_k^*\delta a_{-k}(\omega) + \alpha_{-k}\delta a_k^\dagger(\omega)) + \sqrt{\Gamma}\,b_{-in}(\omega). \tag{29}$$

In the Fourier domain, the temporal correlation of the thermal noise becomes $\frac{1}{2\pi}\int_{-\infty}^{\infty}\langle b_{in}^\dagger(\omega)b_{in}(\omega')\rangle d\omega' = n_q$, where $b_{in}^\dagger(\omega)$ is the Fourier transform of the complex conjugate of $b_{in}(t)$.

S4.4 Brillouin lasing threshold

Below the Brillouin lasing threshold of the co-propagating acoustic wave b_q, the counter-propagating acoustic wave b_{-q} will be damped out. We therefore neglect here the counter-propagating wave b_{-q} in the equations of motion, a valid approximation to predict the dynamics of the forward travelling wave b_q below the lasing threshold. Neglecting the counter-progating wave, the equations of motion are solved using the identity $b^\dagger(\omega) = [b(-\omega)]^\dagger$, and the co-propagating acoustic wave amplitude is:

$$b_q(\omega) = \frac{\sqrt{\Gamma}\,b_{in}(\omega)}{-i(\omega - \Omega_\mathrm{B}) + \Gamma/2 - \frac{g_{0,\mathrm{rp}}g_{0,\mathrm{tot}}n_{cav,k}}{-i\omega+i\Delta+\kappa/2}} \tag{30}$$

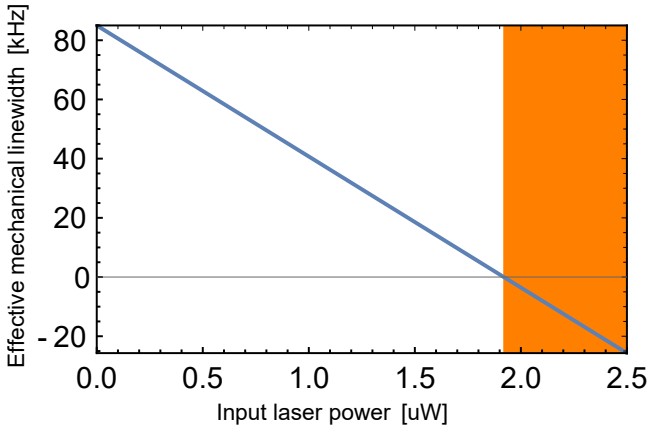

Figure S7: Effective mechanical linewidth Γ_{eff} of the forward propagating acoustic wave versus input laser power (blue line), plotted using Eq. (32). The orange shading corresponds to the region above the Brillouin lasing threshold, for which the analytical theory is no longer valid (see section S5 for above threshold analysis).

We identify the third term in the denominator of Eq.(30) as:

$$\Sigma_{b_q}(\omega) = \frac{-g_{0,\text{rp}} g_{0,\text{tot}} n_{cav,k}}{-i\omega + i\Delta + \kappa/2} = i\delta\Omega_{\text{B}}(\omega) + \frac{\Gamma_{\text{opt}}(\omega)}{2} \tag{31}$$

The imaginary part of $\Sigma_{b_q}(\omega)$ leads to a shift in the Brillouin frequency $\delta\Omega_{\text{B}}$ (optical spring effect), while its real part leads to a modified effective mechanical damping rate Γ_{eff} through the addition of an optical damping term Γ_{opt}. In our system, the total optical cavity linewidth ($\kappa/2\pi = 284$ MHz) is much larger than the acoustic frequency ($\Omega_{\text{B}}/2\pi = 7.3$ MHz) and the pump light is close to resonance ($(\Delta - \omega) \ll \kappa$). As a result, $\Sigma_{b_q} \simeq \text{Re}\{\Sigma_{b_q}\}$ primarily contributes to changing the effective mechanical linewidth through $\Gamma_{\text{opt}} \simeq -\frac{4g_{0,\text{rp}} g_{0,\text{tot}}(n_{cav,k} - n_{cav,-k})}{\kappa_{\text{eff}}}$. The effective mechanical linewidth Γ_{eff} of the co-propagating acoustic wave can thus be expressed as:

$$\Gamma_{\text{eff}} = \Gamma - \frac{4g_{0,\text{rp}} g_{0,\text{tot}}}{\kappa} \zeta n_{cav,k} \tag{32}$$

where the new unitless term, ζ, is added to account for the suppression of linewidth narrowing from backscattered photons. The value of this term is determined via numerical techniques in Sec.S5.

Figure S7 plots Γ_{eff} as a function of input laser power, with the following parameters: acoustic resonance frequency $\Omega_{\text{B}}/2\pi = 7.3$ MHz, laser (pump) frequency $w_L/2\pi = 193$ THz, fiber-to-cavity coupling rate $\kappa_{ext} = 180$ MHz, optical decay rate $\kappa/2\pi = 284$ MHz, the radiation pressure optomechanical coupling rate $g_{0,\text{rp}}$ is estimated to be 11 kHz in Section S1.5 of this supplementary material, optical detuning $\Delta = \Omega_{\text{B}}$, intrinsic mechanical linewidth $\Gamma = 85$ kHz, total optomechanical coupling $g_{0,\text{tot}} = 133$ kHz and $\zeta = 0.22$. The effective linewidth approaches zero at 1.8 μW input power, which corresponds to the Brillouin lasing threshold.

Note as mentioned earlier that this analytical result is only valid in the non-depleted pump regime, and only describes the behaviour below the threshold. The above threshold behaviour is explained by numerically solving the full equations of motion without the non-depleted pump approximation, which accounts for the saturation of the Stokes amplitude (see section S5 for more details).

S4.5 Backreflected light power spectrum

We solve here for the backscattered light power spectrum, used for the solid fit in Fig. 2 of the main text. Following the same approach used to determine b_q, we obtain the backreflected light spectral amplitude $\delta a_{-k}(\omega)$:

$$\delta a_{-k}(\omega) = \frac{i g_{0,\text{rp}} \alpha_k \, b_q^\dagger(\omega)}{-i\omega - i\Delta + \kappa/2} \tag{33}$$

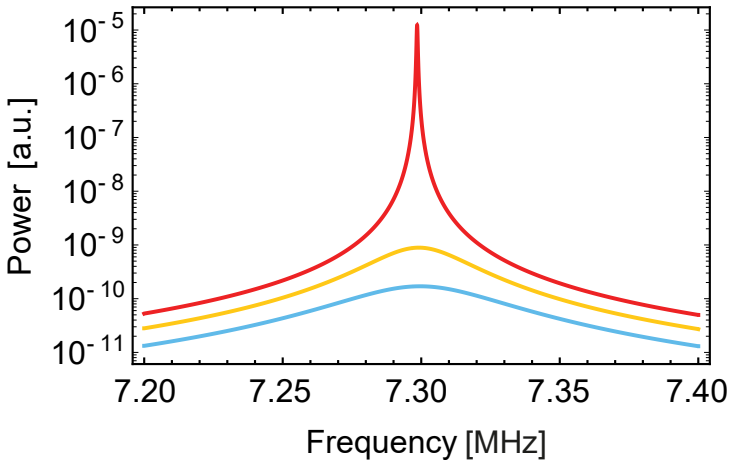

Figure S8: Analytical calculation of the reflected light power spectrum in the non-depleted pump regime, showing the lasing of the Stokes sideband. Curves corrspond to $P_{in} = 0.5\,\mu$W (blue); $P_{in} = 1\,\mu$W (yellow) and $P_{in} = 1.8\,\mu$W (red - at phonon lasing threshold).

The power spectrum of the reflected light then takes the following form using the Wiener-Khinchin theorem:

$$\begin{aligned} S_{\delta a_{-k}\delta a_{-k}}(\omega) &= \frac{1}{2\pi}\int_{-\infty}^{\infty} d\omega' \left\langle [\delta a_{-k}(-\omega)]^\dagger \delta a_{-k}(\omega') \right\rangle \\ &= \frac{1}{2\pi}\int_{-\infty}^{\infty} d\omega' \left\langle \frac{-ig_{0,\mathrm{rp}}\alpha_k^*\, b_q(\omega)}{-i\omega + i\Delta + \kappa/2} \cdot \frac{ig_{0,\mathrm{rp}}\alpha_k\, b_q^\dagger(\omega')}{-i\omega' - i\Delta + \kappa/2} \right\rangle \end{aligned} \tag{34}$$

After substituting the solution of b_q given by Eq.(30) into Eq.(33), the explicit solution of $\delta a_{-k}(\omega)$ is:

$$\delta a_{-k}(\omega) = \frac{ig_{0,\mathrm{rp}}\alpha_k}{-i\omega - i\Delta + \kappa/2} \cdot \left(\frac{\sqrt{\Gamma} b_{in}^\dagger(\omega)}{-i\omega - i\Omega_\mathrm{B} + \Gamma/2 - \frac{g_{0,\mathrm{rp}} g_{0,\mathrm{tot}} n_{cav,k}}{-i\omega - i\Delta + \kappa/2}} \right), \tag{35}$$

where we recognize both an optical cavity and acoustic response components. Defining the cavity susceptibility as $\chi_{-k}(\omega)$ and the Brillouin-interaction modified acoustic susceptibility as $\chi_q(\omega)$, with:

$$\begin{aligned} \chi_{-k}^{-1}(\omega) &= -i\omega - i\Delta + \kappa/2 \\ \chi_q^{-1}(\omega) &= -i(\omega - \Omega_\mathrm{B}) + \Gamma/2 - \frac{g_{0,\mathrm{rp}} g_{0,\mathrm{tot}} n_{cav,k}}{-i\omega + i\Delta + \kappa/2}, \end{aligned} \tag{36}$$

we rewrite the expression of δa_{-k} under the more convenient form:
$\delta a_{-k}(\omega) = ig_{0,\mathrm{rp}}\alpha_k\, \chi_{-k}(\omega)[\sqrt{\Gamma} b_{in}^\dagger(\omega)\chi_q^*(-\omega)]$. The reflected light power spectrum is then reduced to:

$$S_{\delta a_{-k}\delta a_{-k}}(\omega) = g_{0,\mathrm{rp}}^2 n_{cav,k}\Gamma |\chi_{-k}(\omega)|^2 \left[\left|\chi_q^*(-\omega)\right|^2 \cdot (n_q + 1) \right] \tag{37}$$

When the pump power is increased, the co-propagating acoustic wave is increasingly amplified. The Stokes sideband generated by the co-propagating wave is plotted in Fig. S8, using the experimental parameters specified above. The power spectra show how the pump field drives the co-propagating acoustic wave, eventually resulting in lasing around 1.8 μW.

S4.6 Bulk heating from the pump beam

As discussed in the main text, the fountain pressure contribution to the optical forcing arises from superfluid flow induced from optical heating. Given this, one might expect the thermal bath experienced by the acoustic wave to strongly depend on input power. However, the strength of these two effects (i.e. bulk heating and increased forcing) can vary independently, according to material properties and the overlap of the 'hot-spot' to the mechanical mode profile [36, 37]. Indeed, it has been shown that such thermal effects do not necessarily preclude ground state cooling [38].

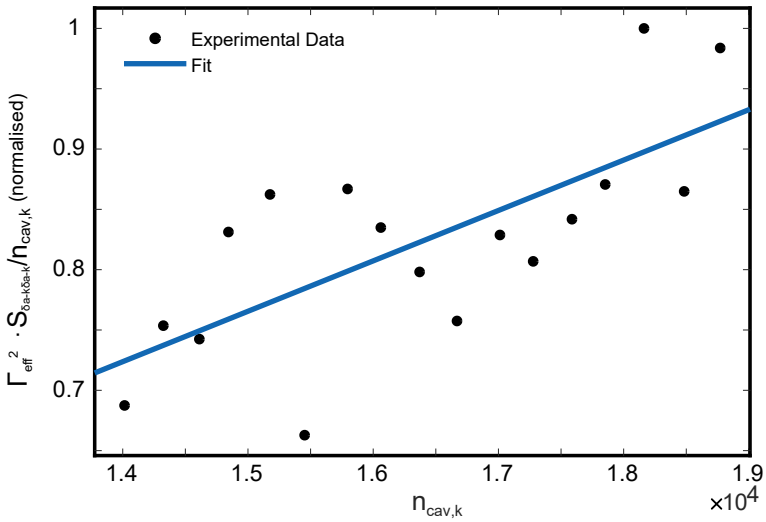

Figure S9: Experimentally observed increase of the thermal bath occupation due to optical absorption in silica. The vertical axis is normalized, and represents the right hand side of Eq. 39. The ratio of the slope to the intercept gives A/n_q.

In the absence of bulk heating, the bath occupancy is related to the Stokes power spectrum and the effective acoustic linewidth. This can be seen by neglecting quantum noise terms and rearranging Eq. 37 with $\omega = \Omega_{\rm B}$,

$$n_q \propto \frac{\Gamma_{\rm eff}^2 S_{\delta a_{-k}\delta a_{-k}}(\Omega_{\rm B})}{n_{cav,k}} \tag{38}$$

This equation shows that, for all pump powers, the RHS of Eq. 38 is constant and related to the bath occupation through a proportionality constant. However, in presence of optical absorption in the silica disk the thermal bath occupancy experienced by the acoustic mode will increase with pump power. Including this passive heating, Eq. 38 becomes:

$$n_q + A\, n_{\rm cav,k} \propto \frac{\Gamma_{\rm eff}^2 S_{\delta a_{-k}\delta a_{-k}}(\Omega_{\rm B})}{n_{\rm cav,k}}, \tag{39}$$

where $n_{\rm cav,k}$ is the intracavity photon number, and A quantifies the conversion from optical photons to acoustic phonons. The product of experimentally measured parameters given on the RHS of Eq. 39 is plotted in Fig. S9. Conveniently, the ratio of the slope to the intercept of the fit is equal to A/n_q, regardless of the measurement efficiency and measurement gains. At the fridge's base temperature (~ 20 mK), with zero input power, the thermal bath occupancy is $n_q \sim 40$. Therefore, from the fitting in Fig. S9, the conversion from optical photons to acoustic phonons is estimated to be $\sim 0.02\%$. For example, just below lasing threshold, at 1.7 μW we have $\sim 2 \times 10^4$ intracavity photons, which will contribute ≈ 400 phonons to the thermal bath.

S5 Full numerical solving of Brillouin equations of motion

Fig. 3 in the main text shows Brillouin lasing as manifested in (a) the fast rise, and subsequent saturation (above $1.8\mu W$), of the Stokes sideband amplitude with increasing input power, and (b) the power spectral density of the back-reflected light for $5.1\mu W$ input power. We illustrate these observations further here by showcasing the time dynamics associated with the spectrum in Fig. 3(b) of the main text. The spectrum and the time-dynamics presented in this section are obtained through numerical integration of the dynamical differential equations of motion (Eqs. 20-23). The analytical expression for the effective linewidth of the Stokes sideband $\Gamma_{\rm eff}$ (Eq. (32), or Eq. (1) in the main text) is valid only in the undepleted pump regime. While this provides an estimate of the power at which the effective mechanical damping $\Gamma_{\rm eff} \to 0$ (the lasing threshold), it breaks down for input powers

Parameter	Symbol	Value	Units
Acoustic damping rate	$\Gamma/2\pi$	85	kHz
Acoustic (Brillouin) frequency	$\Omega_{\mathrm{B}}/2\pi$	6.3	MHz
Laser detuning	Δ	0	MHz
Overall cavity intensity decay rate	$\kappa/2\pi$	284	MHz
Input coupling (external) cavity decay rate	$\kappa_{\mathrm{ext}}/2\pi$	180	MHz
Backscattering decay rate	$\kappa_{\mathrm{b}}/2\pi$	75	MHz
Single photon coupling strength (radiation pressure)	$g_{0,\mathrm{rp}}/2\pi$	11	kHz
Single photon coupling strength (fountain pressure)	$g_{0,\mathrm{fp}}/2\pi$	122	kHz

Table S2: System parameters used in numerical simulation.

exceeding the threshold. Numerical analysis is therefore needed to provide quantitative information in the above-threshold regime. The following system is numerically integrated:

$$\dot{a}_k = i\Delta a_k - \frac{\kappa}{2}a_k + ig_{0,\mathrm{rp}}(b_q + b_{-q}^\dagger)a_{-k} + i\kappa_b a_{-k} + \sqrt{\kappa_{ext}}a_{in} \tag{40}$$

$$\dot{a}_{-k} = i\Delta a_{-k} - \frac{\kappa}{2}a_{-k} + ig_{0,\mathrm{rp}}(b_{-q} + b_q^\dagger)a_k + i\kappa_b a_k \tag{41}$$

$$\dot{b}_q = -i\Omega_{\mathrm{B}}b_q - \frac{\Gamma}{2}b_q + ig_{0,\mathrm{tot}}a_{-k}^\dagger a_k \tag{42}$$

$$\dot{b}_{-q} = -i\Omega_{\mathrm{B}}b_{-q} - \frac{\Gamma}{2}b_{-q} + ig_{0,\mathrm{tot}}a_k^\dagger a_{-k} \tag{43}$$

The simulation parameters and their numerical values are summarized in table S2. With respect to the system Eqs. 20-23, the thermal noise terms $\sqrt{\Gamma}\,b_{-in}(t)$ and $\sqrt{\Gamma}\,b_{in}(t)$ are omitted. While the presence of thermal noise is required in order to seed the lasing process, it can be replaced by non-zero starting conditions. The initialization for the presented simulation was $a_k = a_{-k} = b_q = 0$, and $b_{-q} = 400$. Some initial population (here $|b_{-q}|^2 = 16 \times 10^4$ phonons) in the direction opposite to the pump photons a_k then seeds the Brillouin scattering process. Indeed, the presence of thermal noise and the initialization of the system only has an impact on the very start of the simulation, not on the steady-state lasing dynamics which we are interested in here. It is worth noting here that although the population of pump photons is initialized with $|a_k|^2 = 0$, it rapidly[3] jumps to a finite population set by the coherent laser input field $a_{in} = \sqrt{\frac{P_{in}}{\hbar\omega_L}}$.

Figure S10 shows the evolution over time of the circulating light intensity and acoustic displacement amplitude, in the forward (a and c) and backward (b and d) directions. First, the forward propagating light field is dominant ($|a_k|^2 > |a_{-k}|^2$), and the forward propagating acoustic wave is amplified (shaded region in Fig. S10 c, Stokes process) by reflection of the forward travelling photons. Once this forward-travelling refractive index grating has reached a significant amplitude ($t =\sim 0.005$ s), this leads to a depletion of the pump field a_k, and a saturation of the growth of the lasing forward Brillouin wave b_q. This is the mechanism behind the saturation visible in Fig. 3 (a) of the main text. After some period of transient dynamics ($t =\sim 0.02$ s), the backward propagating acoustic wave (Fig. S10 d) settles into a low amplitude steady-state. The lasing process can also be observed in the frequency domain. The power spectrum of the Brillouin-scattered light $\hat{a}_{-k}$ in Fig. S11 (Fig. 3 (b) in main text) is obtained by taking the Fast Fourier transform over the last 4 ms of the time evolution once the system has reached its steady-state. A local oscillator beam $\hat{a}_{\mathrm{LO}}$ sinusoidally modulated at 80 MHz is added to the signal $\hat{a}_{-k}$ to explicitly mimic the experiment. Aside from the Stokes and anti-Stokes sidebands immediately on either side of the LO, a comb-like pattern is observed, with features integer multiples of the Brillouin frequency Ω_{B} away from the LO. We ascribe these to non-linear sideband mixing and higher-order Stokes scattering. The non-linear mixing is mediated by optical back-scattering, whereby back-scattered pump photons will interfere with Stokes photons and modulate the intensity of the travelling wave grating. This will appear in the power spectrum as harmonics of the original

[3] On a time scale $\sim 1/\kappa \sim$ ns

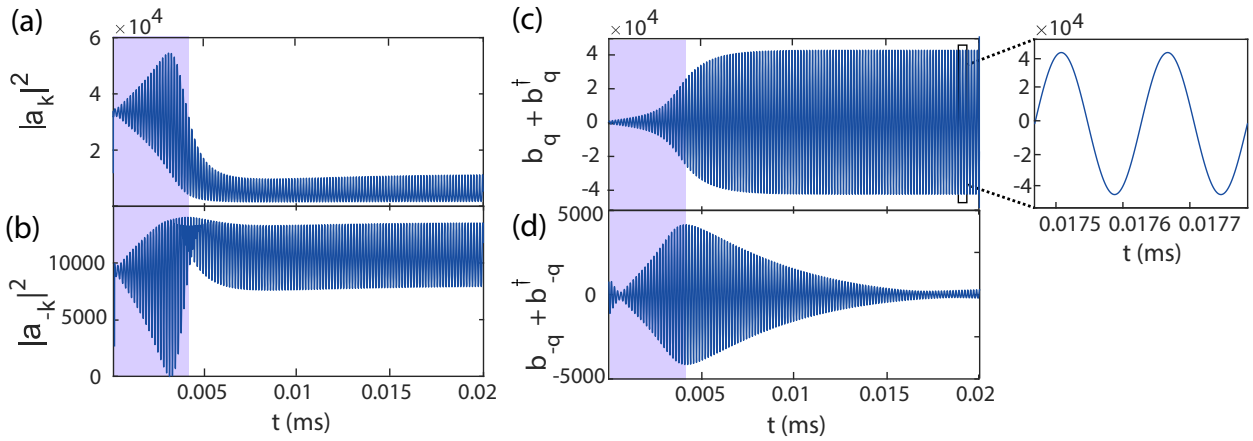

Figure S10: Brillouin scattering at $5.1\mu W$ input power: transient evolution towards steady-state lasing. The field amplitude is a, while $|a|^2$ corresponds to the intracavity photon number. $\hat{b}_q+\hat{b}_q^\dagger$ and $\hat{b}_{-q}+\hat{b}_{-q}^\dagger$ are the displacement amplitudes in units of the zero point fluctuation amplitude $x_{\mathrm{ZPF}} = \sqrt{\hbar/2m\Omega_{\mathrm{B}}}$ [7]. (a) Incoming photons of amplitude $\hat{a}_k$ are converted to (b) backscattered photons of amplitude $\hat{a}_{-k}$ and (c) forward propagating Brillouin phonons with displacement amplitude $\hat{b}_q + \hat{b}_q^\dagger$. (d) Backpropagating acoustic wave with displacement amplitude $\hat{b}_{-q} + \hat{b}_{-q}^\dagger$. Inset: close-up of the Brillouin displacement amplitude in the lasing regime, in a time frame covering two mechanical periods ($2 \times \frac{1}{6.3\,\mathrm{MHz}}$). Plots (a), (b), (c) & (d) show the transient dynamics of a longer $t = 5\,\mathrm{ms}$ simulation with 2×10^7 time steps, used to compute the power spectrum shown in Fig. S11.

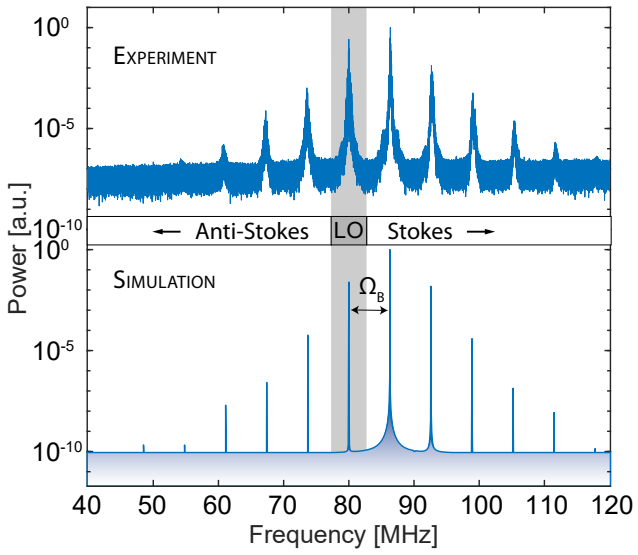

Figure S11: Brillouin lasing observed in the spectrum of light reflected from the cavity at high optical powers. Top: experimental data. Bottom: $|\hat{a}_{-k} + \hat{a}_{\mathrm{LO}}|^2[\omega]$ obtained via numerical integration of differential equations (no free parameters). Frequencies displayed are shifted by a local oscillator beam modulated at 80 MHz. The height of the LO peak is larger in the experiment due to elastic optical backscattering coming e.g. from splices, fiber connections and the fiber taper support pads. These are not taken into account in the simulations, which only account for elastic backscattering due to geometrical imperfections in the resonator (κ_b term).

Stokes line. Comparing the spectral traces in Fig. S11, we observe very good agreement between the experimental observations and theoretical predictions through numerical simulation.

S6 Estimation of electrostrictive $g_{0,\mathrm{es}}$ of the silica disk

We compare here the magnitude of the radiation pressure coupling between light and thickness fluctuations in the superfluid film $g_{0,\mathrm{rp}}$, to the electrostrictive coupling rate between light confined in the silica resonator and an acoustic wave propagating in the silica itself, $g_{0,\mathrm{es\,SiO2}}$. In order to get a rough estimate of $g_{0,\mathrm{es\,SiO2}}$, we consider the silica as an isotropic material whose refractive index only depends on its density. Under this simplifying assumption, the electrostrictive single photon coupling strength $g_{0,\mathrm{es\,SiO2}}$ is given by:

$$g_{0,\mathrm{es\,SiO2}} = \frac{\omega}{2} \frac{\int \gamma_e \, \tilde{\epsilon}_v \left(\vec{r}\right) E_p \left(\vec{r}\right) \, E_s \left(\vec{r}\right) \mathrm{d}^3\vec{r}}{\sqrt{\int \varepsilon E_p \left(\vec{r}\right) \, \mathrm{d}^3\vec{r}} \sqrt{\int \varepsilon E_s \left(\vec{r}\right) \, \mathrm{d}^3\vec{r}}}, \tag{44}$$

where E_p and E_s respectively refer to the pump and Stokes fields, $\tilde{\epsilon}_v = \frac{\delta V_{zp}}{V} = -\frac{\delta \rho_{zp}}{\rho}$ is the zero-point volumetric strain caused by the Brillouin wave in the silica, and $\gamma_e = \left(\rho \frac{\partial \varepsilon}{\partial \rho}\right)_{\rho=\rho_0} = \left(\varepsilon - 1\right)\left(\varepsilon + 2\right)/3$ is the electrostrictive constant of the material [39]. (Thus $\gamma_e \, \tilde{\epsilon}_v$ corresponds to the zero-point permittivity fluctuations of the material due to the Brillouin wave). For backward scattering with identical azimuthal order pump and Stokes waves as is the case in our experiment, Eq.(44) becomes:

$$g_{0,\mathrm{es\,SiO2}} = \frac{\omega}{2} \frac{\int \gamma_e \, \tilde{\epsilon}_v \left(\vec{r}\right) E^2 \left(\vec{r}\right) \, \mathrm{d}^3\vec{r}}{\int \varepsilon E^2 \left(\vec{r}\right) \, \mathrm{d}^3\vec{r}}, \tag{45}$$

We estimate $g_{0,\mathrm{es\,SiO2}}$ through the finite element simulations shown in Fig. S12. Figure S12 (a) and (b) show the optical field distribution of the WGM used in the experiments, while (c) and (d) show the displacement and strain caused by an acoustic wave localized to the silica wedge with $m = 2 \times m_{\mathrm{opt}}$. Estimation of the single photon electrostrictive coupling rate through Eq. 45 yields $g_{0,\mathrm{es\,SiO2}} =\sim 17$ kHz. The radiation pressure contribution due to the moving boundary effect [40] is much smaller, with $g_{0,\mathrm{rp\,SiO2}} =\sim 3$ Hz. The electrostrictive $g_{0,\mathrm{es\,SiO2}}$ for the silica disk is comparable to the radiation pressure $g_{0,\mathrm{rp}}$ due to the moving boundary effect of the superfluid film. The reason we do not observe Brillouin lasing from the silica disk is –beyond the approximatively three orders of magnitude higher acoustic damping rate for the GHz phonons in silica [3] compared to the superfluid sound wave– that it not possible to get 3-fold resonant enhancement (pump+Stokes+acoustic wave) in the silica. Indeed, the Stokes beam would be strongly suppressed in our microresonator as there is a very low density of states for it 10 GHz away from the pump. Typically, the way to get efficient backward Brillouin scattering in a WGM microresonator is for the device's free spectral range (FSR) to match the Brillouin shift (∼10 GHz). This requires a large device size, on the order of 6 mm diameter for silica [41, 42, 3].

Miniaturization would enable large increases in the Brillouin interaction due the efficient co-localization of light and sound, but so far those efforts have been hampered by the fact that the usual energy and momentum matching criteria[4] generally cannot be met in miniaturized devices with sparse optical spectra. However, because of the low speed of superfluid third-sound in our devices, this triple resonant enhancement is automatically satisfied independantly of device size. This approach can be scaled all the way down to devices with λ^3 mode volumes [43], enabling radiation-pressure $g_{0,\mathrm{rp}}/2\pi$ in excess of 10^5 Hz with triply resonant interactions to be achieved.

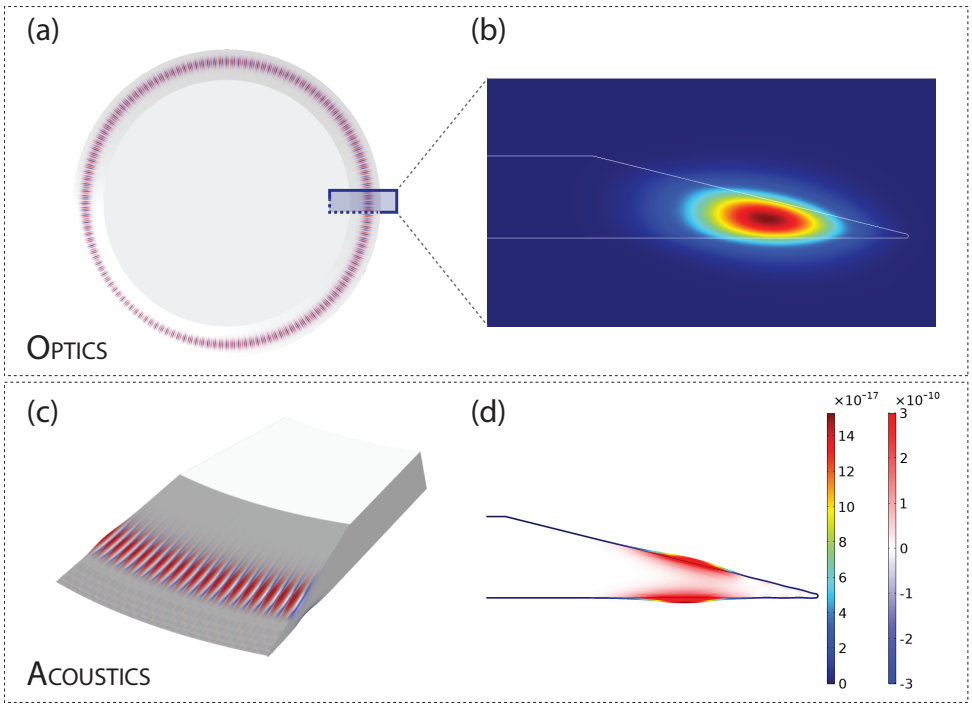

Figure S12: Estimation of the electrostrictive $g_{0,\mathrm{es}}$ of the silica disk resonator. (a) Top-view of the electric field distribution for the ($p = 1$; $m = 186$) TE WGM of the resonator. (b) side-view of the electric field intensity distribution $|E|^2$. (c) Finite element element model of a propagating acoustic wave localized in the disk wedge, with azimuthal order $m = 372$ and frequency $\Omega_{\mathrm{B}} = 6$ GHz. (d) Cross-section of the silica resonator displaying the zero-point surface deflection (line plot), as well as the zero-point volumetric strain (surface plot) due to the Brillouin wave, with their respective scale bars: the zero-point volumetric strain (and relative permittivity) fluctuations are on the order of 10^{-10} while the zero-point surface deflection is on the order of 10^{-16} m.

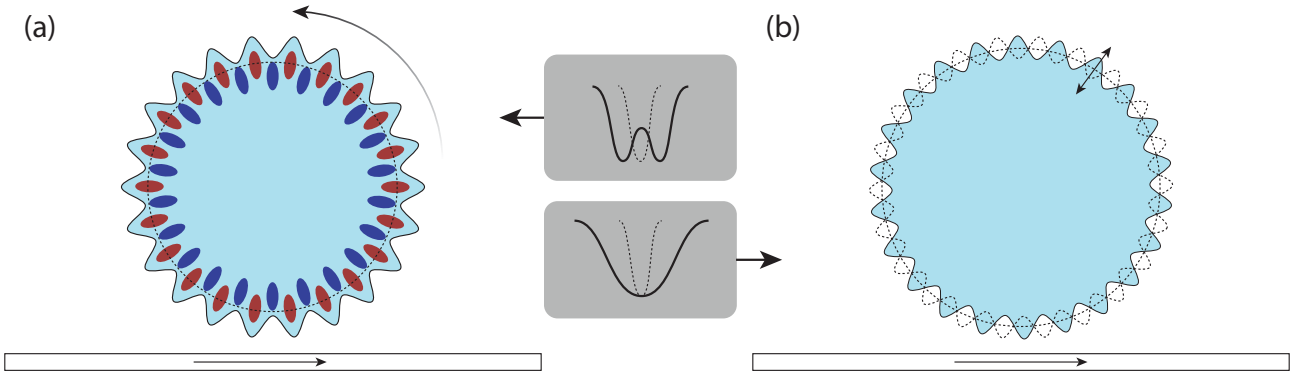

Figure S13: Pump-probe measurement of the cavity optical response, for a travelling wave grating (a), and a stationary oscillating grating (b). While the superfluid film deformation is essentially out-of plane, its localized effect on the effective refractive index is represented here as a localized perturbation to the cavity radius. (a) The initially degenerate CCW and CW WGM resonances are split by the strong Brillouin-induced refractive index grating. The mode splitting can be described in the basis of quasi-stationary modes (red and blue WGMs) rotating at the speed of sound.

S7 Optical strong coupling

S7.1 Experimental measurement of strong optical coupling

The optical spectrum of the cavity is measured with the following pump-probe setup, as illustrated in Figure 1 of the main text. A powerful ($\sim 5\,\mu$W) pump laser (NKT Koheras Adjustik fiber-laser) is brought onto resonance with the initially unsplit cavity WGM resonance. As the pump power is above threshold, this initiates spontaneous Brillouin lasing, as verified through the transmitted light power spectrum. This creates a travelling refractive index grating, as shown in Figure S13(a). This grating travels counterclockwise at the speed of sound, with a frequency $\Omega_{\mathrm{B}}/2\pi \simeq 2\,c_3/\lambda_{\mathrm{light}}$. While the lasing is maintained, a low-power tunable diode laser (Yenista T100S-HP) is repeatedly swept across the optical resonance (100 Hz), using the laser's piezo-wavelength control. The transmitted optical photodetector signal is low-pass filtered (filter bandwidth = 20 kHz) and averaged (256 times) in order obtain the optical cavity spectrum, free from any modulation due to the Brillouin lasing process.

Due to the large refractive index grating generated by the Brillouin lasing process, the probe laser now detects two distinct cavity resonances: a lower frequency resonance (red), where the light intensity is maximal under the peaks of the superfluid wave, and a higher frequency resonance (blue) —spatially shifted by $\lambda_B/2$— corresponding to maximal light intensity under the wave troughs, see Figure S13(a). The magnitude of the measured splitting is a direct measure of the coupling rate g_{opt} between pump and Stokes fields, and for $g_{opt} > \kappa$, strong mechanically mediated optical coupling between CCW and CW optical resonances is achieved.

Note that because the cavity decay rate κ is much larger than the Brillouin frequency Ω_{B} in this scheme, all intracavity photons sense an essentially static refractive index grating, as the grating motion is negligible over the $\sim 1/\kappa$ photon lifetime. Moreover, as the refractive index modulation is simply rotating around the device, the resonance frequencies of red and blue WGMs are essentially constant in time. As such, even though the probe laser sweep-rate is lower than the travelling grating frequency, the photodetector signal can be integrated without loss of information.

In contrast, for an 'optomechanics-like' oscillating stationary refractive index grating (see Figure S13(b)), the magnitude of the measured splitting would now be oscillating in time at frequency $2\Omega_{\mathrm{B}}$. A time-averaged measurement would therefore reveal a broadened optical resonance, with no discernible splitting (see Fig. S13(b) and e.g. Ref. [44]).

S7.2 Theory

Here we calculate the modified eigenfrequencies of a pair of optical cavity modes introduced by mechanically mediated scattering between them.

$$\hat{H} = \hbar\omega_k a_k^\dagger a_k + \hbar\omega_{-k} a_k^\dagger a_{-k} - \hbar g_{0,\mathrm{rp}} \left(a_k^\dagger a_{-k} b_q + a_k a_{-k}^\dagger b_q^\dagger \right), \tag{46}$$

where ω_k and ω_{-k} are the bare eigen frequencies of the two optical modes, and the associated a is the lowering operator of each mode. $g_{0,\mathrm{rp}}$ is the usual vacuum optomechanical coupling rate, and b_q is the lowering operator for the co-propagating acoustic wave, where the counter-propagating wave is neglected. k and q are respectively the wave numbers of the optical modes and acoustic wave, with the signs in the front indicating directions. The bare mechanical Hamiltonian has been neglected here, because we will instead just assume that the mechanical oscillator oscillates at some frequency and at some amplitude (the exact frequency will turn out not to matter, but should be expected to be very close to the bare mechanical resonance frequency).

This Hamiltonian models the Brillouin interaction of particular interest to this experiment, but also a broader class of "photon-phonon translator" type systems such as introduced by the Painter group [45].

[4] Energy and momentum matching conditions in WGM resonators are given by $\omega_{\mathrm{pump}} = \omega_{\mathrm{Stokes}} + \Omega_{\mathrm{B}}$ and $m_B = m_{\mathrm{pump}} \pm m_{\mathrm{Stokes}}$, where + and - respectively correspond to the backward and forward scattering processes.

S7.3 Equations of motion

From the Hamiltonian we directly obtain the equations of motion for the coupled optical cavity modes in the absence of dissipation. While dissipation can have the effect of shifting the eigen mode frequencies, for high quality optical cavities, as is the relevant case for this experiment, this is a negligible effect. Neglecting the dissipation allows a simpler calculation.

The equations of motion are found to be:

$$\dot{a}_k = -i\omega_k a_k + ig_{0,\mathrm{rp}} a_{-k} b_q \tag{47}$$
$$\dot{a}_{-k} = -i\omega_{-k} a_{-k} + ig_{0,\mathrm{rp}} a_k b_q^\dagger \tag{48}$$

Then we treat the mechanical oscillator classically (we're interested in the light scattered due to its coherent oscillation rather than fluctuations) by substituting b_q with $\beta_q e^{-i\Omega_\mathrm{B} t}$. β_q is the amplitude of oscillation and Ω_B can be thought of as the mechanical resonance frequency though in fact our results do not require this (of course, the further away from resonance the harder it will typically be to drive the oscillator to a given amplitude). We take β_q to be real, without loss of generality. This just determines the phase of the mechanical oscillation. Defining the *mechanical-amplitude boosted optomechanical coupling rate* $g_\mathrm{opt} = \beta_q\, g_{0,\mathrm{rp}}$, we then obtain

$$\dot{a}_k = -i\omega_k a_k + ig_\mathrm{opt} e^{-i\Omega_\mathrm{B} t} a_{-k} \tag{49}$$
$$\dot{a}_{-k} = -i\omega_{-k} a_{-k} + ig_\mathrm{opt} e^{i\Omega_\mathrm{B} t} a_k. \tag{50}$$

The terms on the right are coherent coupling terms that act to hybridise the two optical modes. This results in a new pair of orthogonal eigenmodes with shifted frequencies.

To determine the shifted eigenmode frequencies we postulate solutions of the following form:

$$a_k \rightarrow \alpha_k e^{-i\omega t} \tag{51}$$
$$a_{-k} \rightarrow \alpha_{-k} e^{-i\omega t} \tag{52}$$

where ω is the oscillation frequency. Again we are neglecting the fluctuations in the fields, which do not alter the eigenfrequencies, with the α's representing the coherent amplitude of each field. We then find

$$-i\omega a_k = -i\omega_k \alpha_k + ig_\mathrm{opt} e^{-i\Omega_\mathrm{B} t} \alpha_{-k} \tag{53}$$
$$-i\omega a_{-k} = -i\omega_{-k} \alpha_{-k} + ig_\mathrm{opt} e^{i\Omega_\mathrm{B} t} \alpha_k. \tag{54}$$

In matrix representation this can be written as

$$\mathbf{M} \cdot \boldsymbol{\alpha} = \mathbf{0}, \tag{55}$$

where

$$\mathbf{M} = \begin{bmatrix} \omega_k - \omega & -g_\mathrm{opt} e^{-i\Omega_\mathrm{B} t} \\ -g_\mathrm{opt} e^{i\Omega_\mathrm{B} t} & \omega_{-k} - \omega \end{bmatrix}$$

and

$$\boldsymbol{\alpha} = \begin{bmatrix} \alpha_k \\ \alpha_{-k} \end{bmatrix}$$

Non-trivial ($\boldsymbol{\alpha} \neq 0$) solutions to this matrix equation only exist when $\mathbf{M}$ is invertible and has a determinant equal to zero. This gives a condition on the frequency ω:

$$|\mathbf{M}| = (\omega_k - \omega)(\omega_{-k} - \omega) - g_\mathrm{opt}^2 = 0, \tag{56}$$

which does not depend explicitly on the oscillation frequency Ω_B of the mechanical element. Note, there is an implicit dependence, since achieving a large β_q and therefore g_opt is easier for oscillation frequencies near the mechanical resonance frequency. Similarly, choosing appropriate bare optical frequencies can greatly enhance the ability of radiation pressure to drive the mechanical response.

Solving this equation for ω gives two new shifted eigen frequencies $\omega_\pm$ given by

$$\omega_\pm = \bar{\omega} \pm \sqrt{\Delta^2/4 + g^2}, \tag{57}$$

where $\bar{\omega} = (\omega_k + \omega_{-k})/2$ is the average of the two bare resonance frequencies and $\Delta = \omega_k - \omega_{-k}$ is their difference.

We can observe that when $g_{\mathrm{opt}} \gg \Delta$ the splitting between the resonances is given by $\delta = \omega_+ - \omega_- = 2g_{\mathrm{opt}}$ as expected for strong coupling. However, in the reverse regime where $g \ll \Delta$, $\delta = \Delta + 2g_{\mathrm{opt}}^2/\Delta$. In this case, the first term (Δ) is just the initial splitting of the resonances. The shift in splitting due to the mechanically-mediated coupling is $2g_{\mathrm{opt}}^2/\Delta$, suppressed compared to the regime where $g_{\mathrm{opt}} \gg \Delta$ by a factor of Δ/g_{opt}. In this superfluid Brillouin lasing experiment, the initial splitting of the two optical modes is zero, so the strong optical coupling is observed. In contrast, when the initial splitting of the two optical modes is engineered to be the Brillouin shift (typically ~ 10 GHz) in solid Brillouin experiments, it is not possible to obtain strong coupling of the two optical modes.

S7.4 Superfluid wave amplitude in the strong optical coupling regime

As stated earlier, the superfluid acoustic wave-mediated optical coupling strength takes the form:

$$g_{opt} = \beta g_{0,\mathrm{rp}}. \tag{58}$$

Above the Brillouin lasing threshold, with 5.1 μW pump power, the optical splitting in Fig. 3(b) of the main-text gives a mechanically mediated optical coupling rate of $g_{opt}/2\pi = 187.4$ MHz. Combined with a single photon optomechanical coupling rate $g_{0,\mathrm{rp}}/2\pi = 11$ kHz, obtained from fitting the experimental effective acoustic linewidth, this corresponds to a zero-point-motion normalised mechanical amplitude β of 1.9×10^4 (Eq. (58)). This value is of comparable magnitude to that obtained by numerically solving the equations of motion above the lasing threshold (see section S5). Indeed, as shown in Fig. 9(c), in those simulations the acoustic amplitude in the steady-state, with a slightly higher 5.1 μW pump power, is $\sim 4 \times 10^4$ x_{zpf}. With a zero-point-motion amplitude $x_{\mathrm{zpf}} = 9.5 \times 10^{-15}$ m (see Table S1) , these experimental and simulated amplitudes respectively correspond to a deformation of the superfluid interface of 1.8 Å and 3.8 Å.

References

[1] G. I. Harris, D. L. McAuslan, E. Sheridan, Y. Sachkou, C. Baker, and W. P. Bowen, "Laser cooling and control of excitations in superfluid helium," *Nature Physics*, vol. 12, pp. 788–793, Aug. 2016.

[2] D. L. McAuslan, G. I. Harris, C. Baker, Y. Sachkou, X. He, E. Sheridan, and W. P. Bowen, "Microphotonic Forces from Superfluid Flow," *Physical Review X*, vol. 6, p. 021012, Apr. 2016.

[3] H. Lee, T. Chen, J. Li, K. Y. Yang, S. Jeon, O. Painter, and K. J. Vahala, "Chemically etched ultrahigh-Q wedge-resonator on a silicon chip," *Nature Photonics*, vol. 6, pp. 369–373, June 2012.

[4] C. G. Baker, G. I. Harris, D. L. McAuslan, Y. Sachkou, X. He, and W. P. Bowen, "Theoretical framework for thin film superfluid optomechanics: towards the quantum regime," *New Journal of Physics*, vol. 18, p. 123025, Dec. 2016.

[5] F. M. Ellis and H. Luo, "Observation of the persistent-current splitting of a third-sound resonator," *Physical Review B*, vol. 39, no. 4, p. 2703, 1989.

[6] E. Gil-Santos, M. Labousse, C. Baker, A. Goetschy, W. Hease, C. Gomez, A. Lemaître, G. Leo, C. Ciuti, and I. Favero, "Light-Mediated Cascaded Locking of Multiple Nano-Optomechanical Oscillators," *Physical Review Letters*, vol. 118, p. 063605, Feb. 2017.

[7] M. Aspelmeyer, T. J. Kippenberg, and F. Marquardt, "Cavity optomechanics," *Rev. Mod. Phys.*, vol. 86, pp. 1391–1452, Dec 2014.

[8] K. R. Atkins, "Third and Fourth Sound in Liquid Helium II," *Physical Review*, vol. 113, pp. 962–965, Feb. 1959.

[9] L. Ding, C. Baker, P. Senellart, A. Lemaitre, S. Ducci, G. Leo, and I. Favero, "High Frequency GaAs Nano-Optomechanical Disk Resonator," *Physical Review Letters*, vol. 105, Dec. 2010.

[10] S. G. Johnson, M. Ibanescu, M. A. Skorobogatiy, O. Weisberg, J. D. Joannopoulos, and Y. Fink, "Perturbation theory for Maxwells equations with shifting material boundaries," *Physical Review E*, vol. 65, June 2002.

[11] M. A. Woolf, P. M. Platzman, and M. G. Cohen, "Brillouin Scattering in Liquid Helium II," *Physical Review Letters*, vol. 17, pp. 294–297, Aug. 1966.

[12] G. Winterling, G. Walda, and W. Heinicke, "Stimulated brillouin scattering in liquid helium," *Physics Letters A*, vol. 26, pp. 301–302, Feb. 1968.

[13] L. A. D. Lorenzo and K. C. Schwab, "Superfluid optomechanics: coupling of a superfluid to a superconducting condensate," *New Journal of Physics*, vol. 16, p. 113020, Nov. 2014.

[14] A. Kashkanova, A. Shkarin, C. Brown, N. Flowers-Jacobs, L. Childress, S. Hoch, L. Hohmann, K. Ott, J. Reichel, and J. Harris, "Superfluid brillouin optomechanics," *Nature Physics*, vol. 13, no. 1, p. 74, 2017.

[15] Y. P. Sachkou, C. G. Baker, G. I. Harris, O. R. Stockdale, S. Forstner, M. T. Reeves, X. He, D. L. McAuslan, A. S. Bradley, M. J. Davis, and W. P. Bowen, "Coherent vortex dynamics in a strongly-interacting superfluid on a silicon chip," *arXiv:1902.04409 [cond-mat, physics:quant-ph]*, Feb. 2019. arXiv: 1902.04409.

[16] R. J. Donnelly and C. F. Barenghi, "The Observed Properties of Liquid Helium at the Saturated Vapor Pressure," *Journal of Physical and Chemical Reference Data*, vol. 27, pp. 1217–1274, Nov. 1998.

[17] D. R. Tilley and J. Tilley, *Superfluidity and Superconductivity*. CRC Press, Jan. 1990.

[18] F. Souris, X. Rojas, P. Kim, and J. Davis, "Ultralow-Dissipation Superfluid Micromechanical Resonator," *Physical Review Applied*, vol. 7, p. 044008, Apr. 2017.

[19] L. A. De Lorenzo and K. C. Schwab, "Ultra-High Q Acoustic Resonance in Superfluid $$ˆ4$$4he," *Journal of Low Temperature Physics*, vol. 186, pp. 233–240, Feb. 2017.

[20] K. Penanen and R. E. Packard, "A Model for Third Sound Attenuation in Thick 4he Films," *Journal of low temperature physics*, vol. 128, no. 1-2, pp. 25–35, 2002.

[21] J. A. Hoffmann, K. Penanen, J. C. Davis, and R. E. Packard, "Measurements of attenuation of third sound: Evidence of trapped vorticity in thick films of superfluid 4he," *Journal of low temperature physics*, vol. 135, no. 3-4, pp. 177–202, 2004.

[22] R. J. Donnelly, *Quantized vortices in helium II*, vol. 2. Cambridge University Press, 1991.

[23] E. R. Generazio and R. W. Reed, "The scattering of ultrasonic third sound from substrate surface defects," *Journal of low temperature physics*, vol. 56, no. 3-4, pp. 355–377, 1984.

[24] C. Bekker, R. Kalra, C. Baker, and W. P. Bowen, "Injection locking of an electro-optomechanical device," *Optica*, vol. 4, pp. 1196–1204, Oct. 2017.

[25] D. T. Nguyen, C. Baker, W. Hease, S. Sejil, P. Senellart, A. Lematre, S. Ducci, G. Leo, and I. Favero, "Ultrahigh Q-frequency product for optomechanical disk resonators with a mechanical shield," *Applied Physics Letters*, vol. 103, p. 241112, Dec. 2013.

[26] C. A. Condat and T. R. Kirkpatrick, "Third-sound propagation on a periodic substrate," *Physical Review B*, vol. 32, no. 7, p. 4392, 1985.

[27] R. Van Laer, R. Baets, and D. Van Thourhout, "Unifying Brillouin scattering and cavity optomechanics," *Physical Review A*, vol. 93, no. 5, pp. 1–15, 2016.

[28] M. Borselli, T. J. Johnson, and O. Painter, "Beyond the Rayleigh scattering limit in high-Q silicon microdisks: theory and experiment," *Optics Express*, vol. 13, p. 1515, mar 2005.

[29] M. Tomes, F. Marquardt, G. Bahl, and T. Carmon, "Quantum-mechanical theory of optomechanical Brillouin cooling," *Physical Review A - Atomic, Molecular, and Optical Physics*, vol. 84, no. 6, 2011.

[30] G. Bahl, M. Tomes, F. Marquardt, and T. Carmon, "Observation of spontaneous Brillouin cooling," *Nature Physics*, vol. 8, pp. 203–207, mar 2012.

[31] P. Kharel, G. I. Harris, E. A. Kittlaus, W. H. Renninger, N. T. Otterstrom, J. G. E. Harris, and P. T. Rakich, "High-frequency cavity optomechanics using bulk acoustic phonons," aug 2018.

[32] J. Restrepo, J. Gabelli, C. Ciuti, and I. Favero, "Classical and quantum theory of photothermal cavity cooling of a mechanical oscillator," *Comptes Rendus Physique*, vol. 12, no. 9, pp. 860 – 870, 2011. Nano- and micro-optomechanical systems.

[33] M. Pinard and A. Dantan, "Quantum limits of photothermal and radiation pressure cooling of a movable mirror," *New Journal of Physics*, vol. 10, p. 095012, sep 2008.

[34] C. Metzger, I. Favero, A. Ortlieb, and K. Karrai, "Optical self cooling of a deformable fabry-perot cavity in the classical limit," *Phys. Rev. B*, vol. 78, p. 035309, Jul 2008.

[35] W. P. Bowen and G. J. Milburn, *Quantum optomechanics*. CRC Press, 2015.

[36] C. H. Metzger and K. Karrai, "Cavity cooling of a microlever," *Nature*, vol. 432, no. 7020, pp. 1002–1005, 2004.

[37] G. Jourdan, F. Comin, and J. Chevrier, "Mechanical mode dependence of bolometric backaction in an atomic force microscopy microlever," *Physical Review Letters*, vol. 101, no. 13, 2008.

[38] J. Restrepo, J. Gabelli, C. Ciuti, and I. Favero, "Classical and quantum theory of photothermal cavity cooling of a mechanical oscillator," *Comptes Rendus Physique*, vol. 12, no. 9, pp. 860 – 870, 2011. Nano- and micro-optomechanical systems.

[39] R. W. Boyd, *Nonlinear optics*. Elsevier, 2003.

[40] C. Baker, W. Hease, D.-T. Nguyen, A. Andronico, S. Ducci, G. Leo, and I. Favero, "Photoelastic coupling in gallium arsenide optomechanical disk resonators," *Optics Express*, vol. 22, pp. 14072–14086, June 2014.

[41] J. Li, H. Lee, and K. J. Vahala, "Microwave synthesizer using an on-chip Brillouin oscillator," *Nature Communications*, vol. 4, p. 2097, dec 2013.

[42] J. Li, M.-G. Suh, and K. Vahala, "Microresonator brillouin gyroscope," *Optica*, vol. 4, pp. 346–348, Mar 2017.

[43] E. Gil-Santos, C. Baker, D. T. Nguyen, W. Hease, C. Gomez, A. Lematre, S. Ducci, G. Leo, and I. Favero, "High-frequency nano-optomechanical disk resonators in liquids," *Nature Nanotechnology*, vol. 10, pp. 810–816, Sept. 2015.

[44] M. Winger, T. D. Blasius, T. P. Mayer Alegre, A. H. Safavi-Naeini, S. Meenehan, J. Cohen, S. Stobbe, and O. Painter, "A chip-scale integrated cavity-electro-optomechanics platform," *Optics Express*, vol. 19, pp. 24905–24921, Dec. 2011.

[45] A. H. Safavi-Naeini and O. Painter, "Proposal for an optomechanical traveling wave phononphoton translator," *New Journal of Physics*, vol. 13, p. 013017, jan 2011.